Frontiers in Bioscience Landmark

Front. Biosci. (Landmark Ed) **2026**; 31(4): 49504
https://doi.org/10.31083/FBL49504

Original Research

Annexin A5 Regulates Store-Operated Calcium Entry via Glyceraldehyde-3-Phosphate Dehydrogenase in Hepatocellular Carcinoma

Weicheng Gao[1,2], Xiancheng Zhang[1,2], Shuai Ma[1,2], Feiyang Wu[3,*], Xingguo Zhong[1,2,*]

[1]Graduate School, Bengbu Medical University, 233030 Bengbu, Anhui, China
[2]Department of General Surgery, Anhui No. 2 Provincial People's Hospital, 230041 Hefei, Anhui, China
[3]Department of General Surgery, The People's Hospital of Yingshang, 236200 Fuyang, Anhui, China
*Correspondence: wufy98@126.com (Feiyang Wu); zhongxg75@163.com (Xingguo Zhong)
Academic Editor: Amancio Carnero Moya
Submitted: 27 December 2025 Revised: 19 February 2026 Accepted: 11 March 2026 Published: 23 April 2026

Abstract

Background: Hepatocellular carcinoma (HCC) is a major contributor to cancer-related mortality worldwide. Store-operated calcium (Ca^{2+}) entry (SOCE), the principal Ca^{2+} influx pathway in non-excitable cells, has been implicated in regulating tumor cell proliferation, migration, and survival. Although annexin A5 (ANXA5) has been implicated in several malignancies, its mechanistic contribution to Ca^{2+} signaling in HCC remains unclear. **Methods**: SOCE-related differentially expressed genes were identified through integrated bioinformatics analyses of The Cancer Genome Atlas and the Gene Expression Omnibus datasets. Huh-7 and HepG2 cells with stable ANXA5 knockdown were established using lentiviral transduction. Molecular interactions and functional alterations were examined by co-immunoprecipitation, enzymatic activity assays, inositol 1,4,5-trisphosphate (IP_3) quantification, Ca^{2+} imaging, western blotting, quantitative polymerase chain reaction (PCR), and flow cytometry. Cellular phenotypes were assessed using proliferation and migration assays, whereas tumor growth was evaluated in subcutaneous xenograft models using nude mice. Notably, all *in vitro* experiments in this study were validated using both Huh-7 and HepG2 cells, whereas only Huh-7 cells were employed for *in vivo* experiments. **Results**: ANXA5 was identified as an SOCE-associated gene whose elevated expression correlated with poor prognosis in HCC. Functional assays demonstrated that ANXA5 depletion significantly suppressed HCC cell proliferation and migration. Co-immunoprecipitation assays showed reduced levels of GAPDH co-precipitating with ANXA5 in ANXA5-deficient cells, suggesting impaired association between ANXA5 and GAPDH. Although ANXA5 knockdown did not alter GAPDH expression, it markedly reduced GAPDH enzymatic activity, leading to decreased IP_3 production, impaired endoplasmic reticulum Ca^{2+} release, and attenuated SOCE-mediated Ca^{2+} influx. Importantly, pharmacological modulation of phospholipase C (PLC) activity with U73122 and its inactive analog U73443 further supported the involvement of PLC–IP_3 signaling in SOCE impairment and malignant phenotypes following ANXA5 depletion. *In vivo*, ANXA5 silencing significantly inhibited tumor growth and was accompanied by reduced expression of Ki-67, vimentin, and the M2 macrophage marker cluster of differentiation 206 (CD206). **Conclusion**: These findings support a working model in which ANXA5 interacts with GAPDH and is associated with altered IP_3 production and SOCE-dependent Ca^{2+} signaling, potentially contributing to HCC progression and immune modulation. Collectively, this ANXA5/GAPDH/IP_3/SOCE axis may provide a mechanistic framework for understanding HCC development and suggests ANXA5 as a potential therapeutic target.

Keywords: annexin A5; glyceraldehyde-3-phosphate dehydrogenases; inositol 1,4,5-trisphosphate; store-operated calcium entry; hepatocellular carcinoma

1. Introduction

Liver cancer ranks sixth in global cancer incidence and is the third most common cause of cancer-related mortality worldwide, reflecting its substantial fatal burden [1]. Hepatocellular carcinoma (HCC) constitutes the predominant histological subtype, accounting for approximately 85% of primary liver cancers [2]. The development of HCC involves multiple etiological factors, including viral infections, toxin exposure, excessive alcohol consumption, and metabolic disorders [3]. In essence, persistent exposure to these insults subjects hepatocytes to repeated cycles of injury and regeneration, leading to the accumulation of oncogenic mutations that drive malignant transformation [4]. Over the past decades, treatment options for HCC have expanded substantially, encompassing surgery, locoregional interventions, immunotherapy, molecularly targeted therapy, radiotherapy, and chemotherapy, which together have led to improved survival outcomes and a decreased overall cancer burden [2,5,6]. Nevertheless, HCC continues to pose major therapeutic challenges, as reflected by unfavorable long-term prognosis, frequent postoperative recurrence and metastasis, and a 5-year survival rate of approximately 60–80% [7,8]. Nevertheless, HCC continues to pose major therapeutic challenges, as reflected by unfavorable

long-term prognosis, frequent postoperative recurrence and metastasis, and a 5-year survival rate of approximately 60–80%.

Annexin A proteins are a family of calcium (Ca^{2+})-dependent phospholipid-binding proteins that are evolutionarily conserved and present in nearly all eukaryotic organisms. They function by reversibly binding to anionic phospholipids on membrane surfaces in a Ca^{2+}-dependent manner. This fundamental property allows annexins to regulate diverse cellular processes, including inflammation, signal transduction, adhesion, migration, differentiation, proliferation, and apoptosis [9,10]. In vertebrates, annexins are designated annexin A and comprise 12 subtypes (annexins A1–A11 and A13) [11]. Among these, human annexin A5 (ANXA5) is widely expressed in cells and body fluids. It reversibly and specifically binds phosphatidylserine in a Ca^{2+}-dependent manner, performing multiple biological functions. This characteristic is essential for a wide range of physiological and pathological processes, but also enables ANXA5 to serve as a potential targeting agent for cancer therapy [12,13]. ANXA5 has been implicated in tumor metastasis and invasion, promoting cancer progression and angiogenesis [14]. HCC is associated with frequent recurrence, strong metastatic capacity, and unfavorable clinical outcomes. HCC frequently infiltrates the portal vein, forming macroscopic tumor thrombi, which represents a prominent growth pattern in patients with intermediate to advanced-stage disease [14–16]. Notably, ANXA5 is reportedly upregulated in tumor thrombus samples and may represent a candidate biomarker associated with portal vein tumor thrombus formation. Moreover, ANXA5 expression has been associated with lymphatic metastasis [17].

As a ubiquitous intracellular signaling molecule, Ca^{2+} participates in diverse cellular processes such as proliferation, apoptosis, migration, and immune regulation [18,19]. Consequently, the ability of cancer cells to execute malignant functions critically depends on dysregulated intracellular Ca^{2+} homeostasis, which is a well-established driver of tumor initiation, progression, and treatment response [20,21]. Unlike excitable cells, cancer cells lack voltage-gated Ca^{2+} channels and therefore rely on store-operated calcium (Ca^{2+}) entry (SOCE) as the primary pathway for Ca^{2+} influx to support numerous pro-tumorigenic processes [22–24]. SOCE occurs at specialized junctions between the plasma membrane and the endoplasmic reticulum (PM–ER), where the local lipid composition—specifically phosphatidylinositol-(4,5)-bisphosphate (PI(4,5)P2, PIP_2)—plays a critical role in maintaining structural stability [25,26]. The activation of SOCE is initiated by the cleavage of PIP_2 by phospholipase C (PLC) to generate inositol 1,4,5-trisphosphate (IP_3), which binds to IP_3 receptors on the ER membrane, depleting ER Ca^{2+} stores and triggering Ca^{2+} influx [27,28]. Dysregulation of this pathway has been implicated in tumor progression; however, the upstream regulators of SOCE, including annexins, remain incompletely understood. Notably, ANXA5 can form a complex with phosphatidylinositol phosphate kinase gamma (PIPKIγ) to control local PIP_2 abundance [29–32]. By modulating PIP_2 levels, ANXA5 is positioned to influence both the structural integrity of PM–ER junctions and the generation of IP_3, thereby regulating SOCE-mediated Ca^{2+} entry.

Based on our study and current mechanistic knowledge, we propose a model where ANXA5 regulates SOCE-mediated Ca^{2+} signaling in HCC. Specifically, decreased GAPDH activity is expected to impair the production of phosphoinositides (PPIs), as their synthesis depends on metabolic pathways (glycolysis, gluconeogenesis, and the pentose phosphate pathway) driven by GAPDH's catalytic function [33–36]. ANXA5 may modulate PIP_2 synthesis by regulating GAPDH enzymatic activity, which in turn affects the Warburg effect—the primary metabolic pathway in tumor cells—thereby altering PPI availability. In addition, ANXA5 can interact with PIPKIγ to further control PIP_2 abundance at the PM. These coordinated interactions are hypothesized to facilitate the assembly and stabilization of PM–ER junctions, ultimately promoting SOCE-dependent Ca^{2+} influx.

Our observations support a model in which ANXA5 regulates HCC malignancy by bridging metabolism, Ca^{2+} signaling pathways, and tumor-related immunity. In this study, we investigated the molecular framework linking ANXA5 to GAPDH activity, PIP_2 metabolism, PM–ER junction formation, and SOCE function, as well as its potential impact on macrophage polarization. Understanding these mechanisms may provide novel insights into HCC biology, positioning ANXA5 as a promising target for therapeutic intervention. The proposed mechanism is illustrated in Fig. 1.

2. Materials and Methods

2.1 Data Acquisition

Data acquisition involved three steps. First, HCC gene expression profiles and matched clinical data were acquired from The Cancer Genome Atlas (TCGA; https://www.cancer.gov), including 424 tissue samples (374 tumor, 50 normal) and corresponding clinical data for 377 patients. Second, survival-specific expression data for 118 HCC cases were independently obtained from the Gene Expression Omnibus (GEO) dataset (GSE10186; https://www.ncbi.nlm.nih.gov). Third, a list of 246 SRGs was generated by screening the GeneCards database (https://www.genecards.org), retaining only genes with a relevance score >15 [37]. The matrix data pertaining to TCGA, GEO, and SRGs are comprehensively detailed in the Appendix.

2.2 Differentially Expressed Genes Associated With Survival

Bioinformatics analysis was conducted using Perl (v5.30.0) and R (v4.3.2). Gene expression data were for-

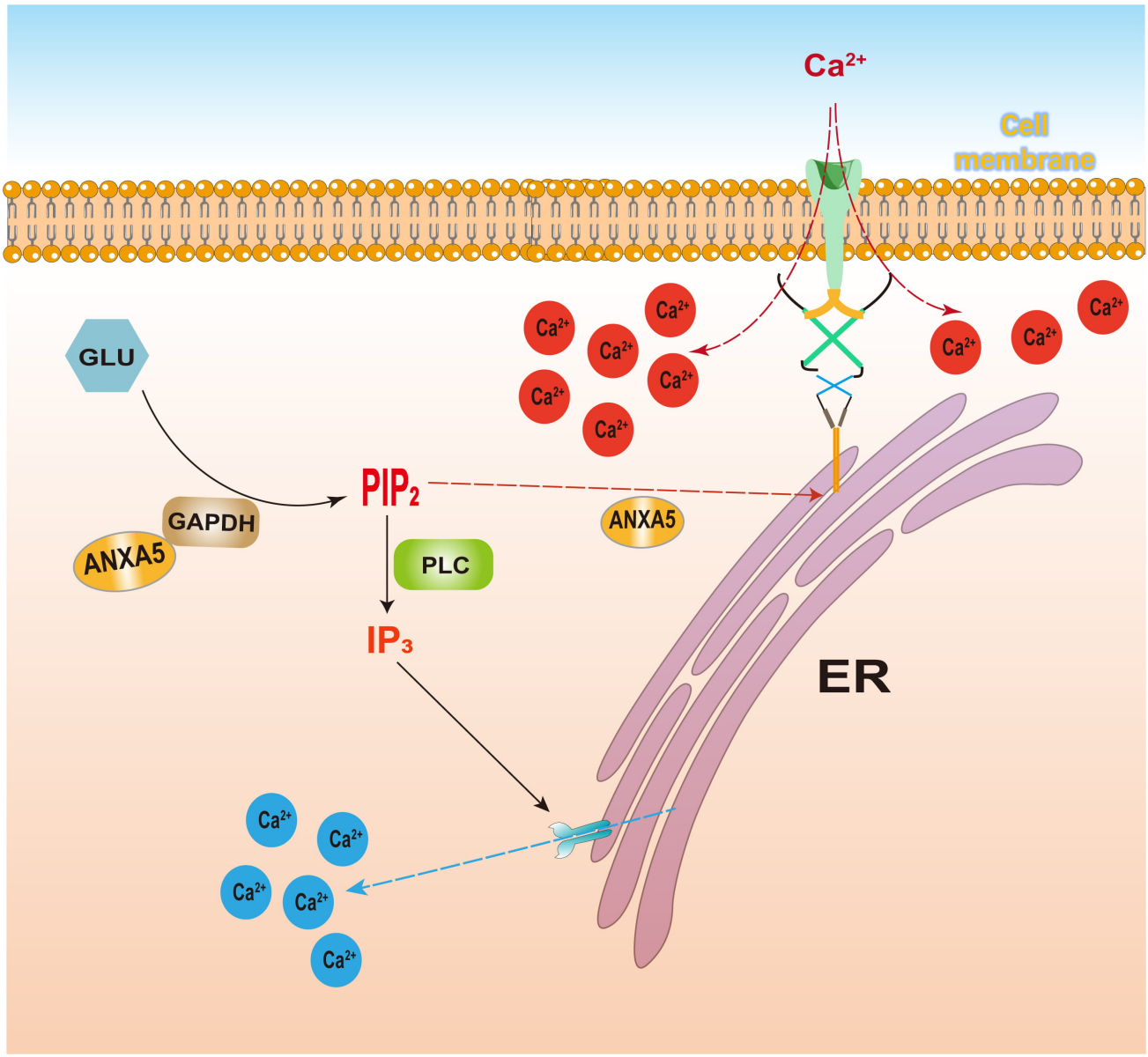

Fig. 1. ANXA5 regulates the SOCE pathway. ANXA5, annexin A5; SOCE, store-operated calcium (Ca^{2+}) entry. This figure was created using Adobe Illustrator 2023.

matted into a matrix, featuring genes as rows and samples as columns. For genes with multiple probes, expression values were averaged to produce a single value per gene. Genes with zero mean expression across all samples were removed. Finally, the analysis was limited to the intersection of this filtered expression matrix and the curated SRG set. Differential expression analysis between normal and tumor tissues was conducted using the Wilcoxon rank-sum test. Differentially expressed genes (DEGs) were defined as those with a false discovery rate (FDR) <0.05 and logFC >1. These DEGs were subsequently subjected to downstream functional and prognostic evaluations. Univariate Cox proportional hazards regression analysis was used to evaluate the impact of gene expression on overall survival (OS). Genes with a Cox p-value < 0.05 were considered significantly associated with prognosis. Hazard ratios (HRs) and 95% confidence intervals (CIs) were calculated for each. Results were visualized using forest plots, with HR >1 indicating risk factors and HR <1 indicating protective factors.

2.3 Cluster Analysis

Tumor transcriptomic data from TCGA (https://www.cancer.gov) and GEO (https://www.ncbi.nlm.nih.gov), encompassing survival-associated gene expression profiles, were subjected to molecular subtyping using an unsupervised consensus clustering approach. This was implemented via the ConsensusClusterPlus R package with the following parameters: clusterAlg = "km", 80% pItem = 0.8, pFeature = 1, and reps = 500 to ensure robustness. The con-

sensus matrix and cumulative distribution function (CDF) were evaluated across a predefined range of cluster numbers (k = 2 to 9) to determine the optimal k value. The optimal number of stable clusters (k = 2) was selected based on the criteria of maximal intercluster divergence and intracluster concordance, as reflected by the consensus matrix heatmap and relative change in area under the CDF curve. The resulting subtypes were designated Cluster A and Cluster B. Subsequently, to evaluate the prognostic value of the identified subtypes, we integrated OS data. Survival differences between clusters were visualized using Kaplan–Meier analysis and statistically compared via the log-rank (Mantel-Cox) test. Furthermore, HRs and their CIs were also determined using a univariate Cox proportional hazards model, with all analyses conducted using the survival and survminer R packages.

2.4 Construction of a Prognostic Risk Model

To develop a prognostic risk signature based on SRGs, a combination of least absolute shrinkage and selection operator (LASSO) regression and multivariate Cox proportional hazards regression was employed. The data were randomly divided into training (70%) and testing (30%) sets using the caret package in R, which was used for all statistical analyses. To identify genes linked to survival, a LASSO-penalized Cox proportional hazards model was applied to the training cohort using the glmnet package. The optimal regularization parameter (λ) was selected based on the minimum criteria within a 10-fold cross-validation framework. Genes with non-zero coefficients at optimal λ (lambda.min) were selected to refine the list. Multivariate Cox proportional hazards regression analysis was performed on these retained genes to construct the definitive prognostic model. To refine the model, bidirectional stepwise regression (in both directions) was performed, and the resulting final multivariate Cox model was used to calculate a prognostic risk score for each patient (Mathematical Components 1).

$$Risk\ score = \sum_{i=1}^{n} Coef_i \times x_i \tag{1}$$

$Coef_i$ represents the correlation coefficient of prognostic genes; x_i represents the expression of prognostic genes. Ultimately, multivariate Cox regression analysis was conducted to determine significant clinical prognostic genes.

$$\text{Surv(futime, fustat)} = \text{Age} + \text{Sex} + \text{Stage} + \text{RiskScore} \tag{2}$$

$$GAPDH_{\text{activity}}\ (U/\text{mg prot}) = \frac{\Delta A}{\varepsilon \times d} \times 10^9 \times \frac{V_{\text{total}}}{V_{\text{sample}} \times C_{\text{pr}}} \times \frac{1}{T} \tag{3}$$

The absorbance at 340 nm was recorded immediately (A_1), and again after a 5-min incubation at 37 °C (A_2). $\Delta A = A_1 - A_2$; ε = molar extinction coefficient of NADH at 340 nm (6.22 $\times$ 10^3 L/mol/cm); d = light-path length (0.6 cm for a 96-well UV plate); V_{total} = total reaction volume (0.2 mL); V_{sample} = volume of sample added to the reaction (0.006 mL); C_{pr} = protein concentration of the sample (mg/mL); T = reaction time (5 min); 10^9 = 1 mol = 10^9 nmol.

$$F/F_0 = \frac{F_t}{F_0} \tag{4}$$

Here, F_0 represents the baseline fluorescence intensity prior to stimulation, and F_t represents the fluorescence intensity at time t. The resulting F/F_0 versus time curves were used to characterize dynamic intracellular Ca^{2+} responses.

Using the median training set risk score as a cutoff, patients in both the training and testing cohorts were stratified into high- and low-risk groups. Survival differences between these groups were assessed using the log-rank test. Time-dependent receiver operating characteristic (ROC) analysis (timeROC package) was conducted to assess the 3-year prognostic accuracy of the model. The model was validated across both cohorts based on specific performance metrics: training set (log-rank $p < 0.01$, AUC >0.68) and testing set ($p < 0.05$, AUC >0.65).

2.5 Survival and ROC Analyses

The prognostic capacity of the risk score was assessed separately in the training, testing, and combined cohorts. For each cohort, OS probabilities between the predefined high- and low-risk groups were estimated via the Kaplan–Meier method. To evaluate the statistical significance of survival differences, the log-rank (Mantel-Cox) test was employed, with survival curves visualized with the survminer package. To quantify the time-dependent predictive accuracy of the risk score, a time-dependent ROC analysis was performed using the timeROC package. This analysis was conducted at three clinically relevant time points: 1, 3, and 5 years post-diagnosis. To evaluate the model's discriminative power, the area under the curve (AUC) and its 95% CIs were calculated for each time point. A custom function was used to plot all three ROC curves on a single graph.

2.6 Independent Prognostic Analysis

To assess whether the SRG-derived risk score serves as an independent predictor of OS, multivariate Cox proportional hazards regression analysis was performed. Clinical covariates (including age, sex and tumor stage) were incorporated alongside the continuous risk score. Prior to analysis, samples with any missing clinical information (coded

Table 1. Negative control and three experimental control gene sequences.

No.	Lentiviral vector name	Gene sequence
1	shRNA-NC	5′-GGGTGAACTCACGTCAGAA-3′
2	shRNA-ANXA5(h)-1	5′-GCATCCTGACTCTGTTGACAT-3′
3	shRNA-ANXA5(h)-2	5′-GCCATCAAACAAGTTTATGAA-3′
4	shRNA-ANXA5(h)-3	5′-CGCGAGACTTCTGGCAATTTA-3′

shRNA, short hairpin RNA; NC, negative control.

as "unknown") were excluded. To ensure a consistent, matched cohort, only samples present in both the risk score and complete clinical datasets were retained. The Cox proportional hazards model, defined by Mathematical Components 2, was then fitted using a combined dataframe that included survival time (futime), status (fustat), all clinical variables, and the riskScore (Mathematical Components 2). HRs, 95% CIs, and Wald test *p* were extracted for each variable from the fitted model, and then summarized and exported. Finally, a forest plot was generated using the ggforest function from the survminer package to visually present the HRs and 95% CIs of all covariates, with the risk score highlighted.

To visually depict the expression profiles of the signature genes across the patient cohort, a heatmap was constructed using the pheatmap package. Patients were sorted by ascending risk order, after which the model gene expression matrix was extracted and transposed to align genes as rows and ordered patients as columns. To visualize relative expression patterns, row-wise z-score normalization (scale = "row") was applied and mapped to a continuous blue-white-red color scale.

2.7 Nomogram Construction and Calibration

A prognostic nomogram was developed using the regplot package to provide quantitative estimates of 1-, 3-, and 5-year OS. This tool was based on a final multivariate Cox proportional hazards model that incorporated all significant independent predictors, including clinical variables and the continuous risk score. To assess the accuracy of the nomogram's predictions, calibration curves were generated for the same three time points using the rms::calibrate function with 1000 bootstrap iterations. This method compares the predicted survival probabilities against the observed Kaplan–Meier estimates to determine performance. The model's goodness-of-fit was visually verified by the proximity of the calibration curves to the 45-degree line. Cumulative hazard curves (via survminer::ggsurvplot with fun = "cumhaz") were used to compare risk over time between groups divided by their median nomogram score. Prior to all analyses, data integrity was ensured by excluding samples with any missing clinical information and retaining only those patients present in both the risk score and clinical datasets.

2.8 Key Gene Filtration

To explore the immune microenvironment associated with high-risk genes, immune cell enrichment analysis was performed leveraging the Tumor Immune Single Cell Hub 2 (TISCH2) database (https://tisch.compbio.cn/gallery/). Separately, to elucidate the functional interactions among these genes, a protein–protein interaction network was constructed. The network data were retrieved from the STRING database (version 12.0; https://cn.string-db.org/), applying a minimum required interaction confidence score threshold to filter for high-confidence interactions. The resulting network was subsequently imported into Cytoscape software (version 3.9.0) for advanced visualization and topological analysis, enabling clearer representation of molecular interaction hubs and modules [38].

2.9 Cell Culture

The human HCC cell lines Huh-7 (STCC10102; Servicebio, Wuhan, China) and HepG2 (STCC10114P; Servicebio) were cultured in Dulbecco's Modified Eagle Medium (DMEM, G4511-500ML; Servicebio) supplemented with 10% fetal bovine serum (FBS, FSP500; ExCell Bio, Shanghai, China) and 1% penicillin–streptomycin (G4003; Servicebio). Cells were maintained under standard conditions at 37 ℃ in a 5% CO_2 humidified atmosphere, with daily monitoring of confluence and morphology, ensuring optimal growth before subsequent experimental use. Both Huh-7 and HepG2 cell lines have been authenticated by STR profiling and confirmed to be mycoplasma-negative.

2.10 Cell Transfection

To investigate the functional impact of ANXA5, Huh-7 and HepG2 cells were transduced with a recombinant lentiviral vector targeting ANXA5 (single hairpin RNA [shRNA]-ANXA5; Genebio, Shanghai, China). A non-targeting, scrambled shRNA lentivirus (shRNA-negative control [NC]) was used as the NC.

The specific shRNA sequences are listed in Table 1. Briefly, Huh-7 and HepG2 cells were seeded in 6-well plates; at approximately 80% confluence, they were transduced with lentiviruses in a mixture of DMEM and polybrene (40804ES76; Yeasen, Shanghai, China). After 12 h, the transduction mixture was replaced with fresh complete culture medium. Following an additional 3–4 days of culture, stable cell pools were selected using puromycin (HY-

Table 2. qPCR primers used in this study.

Species	Gene	Forward primer (5′ to 3′)	Reverse primer (5′ to 3′)
Human	*ACTIN*	CACCCAGCACAATGAAGATCAAGAT	CCAGTTTTTAAATCCTGAGTCAAGC
Human	*ANXA5*	GACTTCCCTGGATTTGATGAGC	GAGGGTTTCATCAGAGCCACAA
Human	*GAPDH*	GGAAGCTTGTCATCAATGGAAATC	TGATGACCCTTTTGGCTCCC

qPCR, quantitative Polymerase Chain Reaction.

K1057; MedChemExpress, Shanghai, China) over a 3- to 4-day period. Transduction efficiency was initially assessed by observing green fluorescent protein expression under a fluorescence microscope. The knockdown (KD) efficiency of ANXA5 was subsequently confirmed at the mRNA and protein levels using quantitative PCR (qPCR) and Western blotting, respectively. All procedures were performed according to the manufacturer's protocol (Genebio) and established laboratory methods [39,40].

2.11 Western Blot Analysis

Total protein was isolated from control and transfected cells (Huh-7 and HepG2) with RIPA lysis buffer (G2002-100ML; Servicebio). Following extraction, lysates were clarified by centrifugation at 12,000 rpm for 10 min at 4 °C. The protein concentration in the supernatants was quantified using a BCA assay kit (G2026-200T; Servicebio). Equal protein concentrations were resolved by 10% sodium dodecyl sulfate polyacrylamide gel electrophoresis (SDS-PAGE) and electrotransferred onto PVDF membranes. After blocking in 5% non-fat milk for 30 min at room temperature, the membranes were probed overnight at 4 °C with primary antibodies against ANXA5 (1:1000, 11060-1-AP; Sanying, Wuhan, China), GAPDH (1:1000, GB15004; Servicebio), and β-actin (1:5000, GB15003; Servicebio). Post-incubation, membranes were washed three times with Tris-buffered saline with Tween 20 and then incubated with horseradish-peroxidase (HRP)-conjugated goat anti-rabbit secondary antibody (1:5000, GB23303; Servicebio). Signal detection was performed using an enhanced chemiluminescence substrate, and bands were imaged on X-ray film.

2.12 Co-Immunoprecipitation Assays

Co-immunoprecipitation (Co-IP) assays were performed to assess the interaction between ANXA5 and GAPDH under different ANXA5 expression conditions. Huh-7 and HepG2 cells from the wild-type (WT), NC, and ANXA5-KD groups were lysed using ice-cold IP lysis buffer supplemented with protease inhibitors. After centrifugation at 12,000 ×g for 15 min at 4 °C, the clarified supernatants were collected, and protein concentrations were quantified by the BCA assay. Equal amounts of total protein from each group were incubated overnight at 4 °C with an anti-ANXA5 antibody (IP-grade) or control IgG under gentle rotation. Protein A/G agarose beads were then added and incubated for an additional 2–4 h to capture immune complexes. The beads were washed repeatedly with lysis buffer to reduce nonspecific binding. IP'd proteins were eluted by boiling in SDS sample buffer and subjected to SDS-PAGE, followed by electrotransfer to PVDF membranes. Western blotting was performed using an anti-GAPDH antibody (Western blot-grade) to detect co-precipitated proteins. A fraction of whole cell lysate (input) was included to verify protein expression levels across different groups.

2.13 Quantitative PCR (qPCR)

Total RNA extraction was performed using TRIzol Reagent (G3013; Servicebio) on control and transfected cells samples (Huh-7 and HepG2). RNA quality was determined by spectrophotometry. Subsequently, cDNA was synthesized from the RNA templates with the SweScript All-in-One RT SuperMix Kit (G3337; Servicebio). Gene expression was quantified by qPCR using the 2× Universal Blue SYBR Green qPCR Master Mix (G3326; Servicebio) and the $2^{-\Delta\Delta CT}$ calculation method. The specific primers utilized are listed in Table 2.

2.14 Cell Counting Kit-8

Following trypsinization and resuspension in complete medium, control and transfected cells (Huh-7 and HepG2) were plated in 96-well plates at a density ranging from 5×10^3 to 5×10^4 cells per well. After a 24-h incubation under standard conditions (37 °C, 5% CO_2), 10 µL of Cell Counting Kit-8 (CCK-8, G4103-5; Servicebio) reagent was added to each well. Then the plates were incubated for an additional 4 h, after which the absorbance at 450 nm was recorded using a microplate reader to assess cell viability.

2.15 Enzyme-Linked Immunosorbent Assay

The enzymatic activity of GAPDH in cultured control and transfected cells (Huh-7 and HepG2) were measured using a commercial GAPDH activity assay kit (BC2215; Solarbio) according to the manufacturer's instructions [41]. GAPDH activity was expressed as units per mg of protein, where one unit was defined as the amount of enzyme that oxidizes 1 nmol of NADH per minute under the assay conditions. For measurements performed in a 96-well ultraviolet (UV) plate (light path = 0.6 cm), activity was calculated using Mathematical Components 3.

For IP_3 quantification, control and transfected cells (Huh-7 and HepG2) lysates were prepared, and a standard curve was established using serial dilutions of the supplied standard. The biotinylated detection antibody and HRP

conjugate were diluted to 1× working solutions according to the manufacturer's instructions. The enzyme-linked immunosorbent assay (ELISA) assay was conducted using a commercial kit (E-EL-0059; Elabscience, Wuhan, China) following the recommended protocol. Briefly, 50 µL of standards or cell lysates were added to a 48-well plate, followed by 50 µL of 1× biotinylated antibody. Following a 45-min incubation, the wells were washed three times with phosphate-buffered saline (PBS). Next, 100 µL of diluted HRP conjugate was added and incubated for 30 min, after which the plate was washed five times. Following the addition of 90 µL of substrate solution, the reaction was incubated for 30 min and then terminated with the stop solution. The absorbance was subsequently measured at 450 nm using a microplate reader [42].

2.16 PLC–IP_3 Pathway Modulation Assay

For rescue and inhibition assays, Huh-7-WT and HepG2-WT cells were assigned to three groups: vehicle control (dimethyl sulfoxide [DMSO] (GC203006-10 mL; Servicebio), PLC inhibitor-treated (U73122, HY-13419; MedChemExpress) and inactive analog-treated (U73343, HY-108630; MedChemExpress), However ANXA5-KD (Huh-7-ANXA5 and HepG2-ANXA5) was another group. For pharmacological modulation, above three groups WT cells were pretreated with U73122 or U73443 (5 µM) for 30 min prior to subsequent analyses, whereas control cells received an equivalent volume of DMSO (<0.1%). After treatment, intracellular IP_3 levels of four were quantified by ELISA according to the manufacturer's instructions.

2.17 Intracellular Ca^{2+} Measurement

Control and transfected cells (Huh-7 and HepG2) were seeded into black 96-well clear-bottom plates at a density of 1×10^5 cells per well and cultured for 24 h. After two to three washes with PBS, cells were loaded with 5 µM Rhod-4 AM (indicator used to detect intracellular Ca^{2+}, MX4508-50UG; Maokangbio, Shanghai, China) premixed 1:1 (v/v) with 20% (w/v) Pluronic F-127 (MS4301-1G; Maokangbio), resulting in a final Pluronic concentration of 0.02%. Cells were incubated with this solution at 37 °C for 30 min, followed by three washes with Ca^{2+}-free Ringer solution.

Fluorescence measurements were recorded using the SpectraMax iD3 multi-mode microplate reader (MD SpectraMax iD3; Molecular Devices, Shanghai, China) with a 540 ± 10 nm excitation filter and a 590 nm emission filter, acquiring signals every 2 s. Baseline fluorescence (F_0) was recorded for 0–60 s. At 60 s, ATP (D7378-2ml; Beyotime, Shanghai, China) (100 µM) in Ca^{2+}-free Ringer solution (155 mM NaCl, 4.5 mM KCl, 3 mM $MgCl_2$, 10 mM D-glucose, 5 mM Na-HEPES) was applied to induce ER Ca^{2+} store depletion, and fluorescence was monitored from 60 to 154 s. Subsequently, 2 mM $CaCl_2$ was added (final $[Ca^{2+}]$ = 1 mM) to trigger SOCE, which was recorded from 154 to 430 s. The total recording duration was 0–600 s.

For each well, time-dependent fluorescence intensity (F_t) was collected, and intracellular Ca^{2+} changes were expressed as the ratio (Mathematical Components 4).

2.18 Wound Healing Assay

Cell migratory capacity was evaluated using a wound healing assay. WT, NC, and ANXA5-KD cells (Huh-7 and HepG2) were plated in 6-well plates at a density of 5×10^5 cells per well and grown to complete confluence. A straight scratch was generated across the cell monolayer using a sterile 200 µL pipette tip. After gentle washing to remove detached cells, cultures were maintained in medium containing a reduced serum concentration. Images of identical wound regions were acquired immediately after scratching and again at 48 h. Cell migration was quantified by calculating the change in wound width with ImageJ software (National Institutes of Health, Bethesda, MD, USA).

2.19 Cell Apoptosis by Flow Cytometry

Apoptosis was evaluated by flow cytometry using an Annexin V-FITC/PI apoptosis detection kit (BL107B; Biosharp, Guangzhou, China). To ensure inclusion of detached apoptotic cells, both culture supernatants and adherent cells were collected. Control and transfected cells (Huh-7 and HepG2) were detached with EDTA-free trypsin (G4002-100ML; Servicebio) to avoid nonspecific staining, followed by centrifugation at 2000 ×g for 5 min. After removal of the supernatant, cell pellets were washed twice with ice-cold PBS and resuspended in 500 µL of 1× binding buffer at a final concentration of 1×10^6 cells/mL. Then cells were incubated with Annexin V-FITC and propidium iodide for 15 min at room temperature in the dark in accordance with the manufacturer's instructions. Flow cytometry was conducted immediately after staining.

2.20 Nude Mouse Xenograft Model

All animal procedures were reviewed and approved by the Animal Care and Use Committee of Bengbu Medical University (Approval No. [2025]514), and conducted in compliance with relevant institutional and national regulations. Fifteen male BALB/c nude mice (3 weeks old) obtained from Jiangsu Cavens Biotechnology (Shanghai, China) were randomly assigned to three groups (n = 5 per group): Huh-7-WT, Huh-7-NC, and Huh-7-ANXA5. Due to constraints in time and resources, the study was conducted exclusively with Huh-7 cells, representing a potential experimental limitation. For xenograft establishment, mice were anesthetized with isoflurane (induction at 3–4% and maintenance at 1.5–2% in oxygen, administered via inhalation; Hengfeng Qiang Biotechnology Co., Ltd., Jiangsu, China, batch No. 2401) and 5×10^6 corresponding cells suspended in 100 µL of DMEM were injected subcutaneously into the right flank. Tumor growth and body weight were monitored daily. After a 3-week experimental period, animals were deeply anesthetized with isoflurane

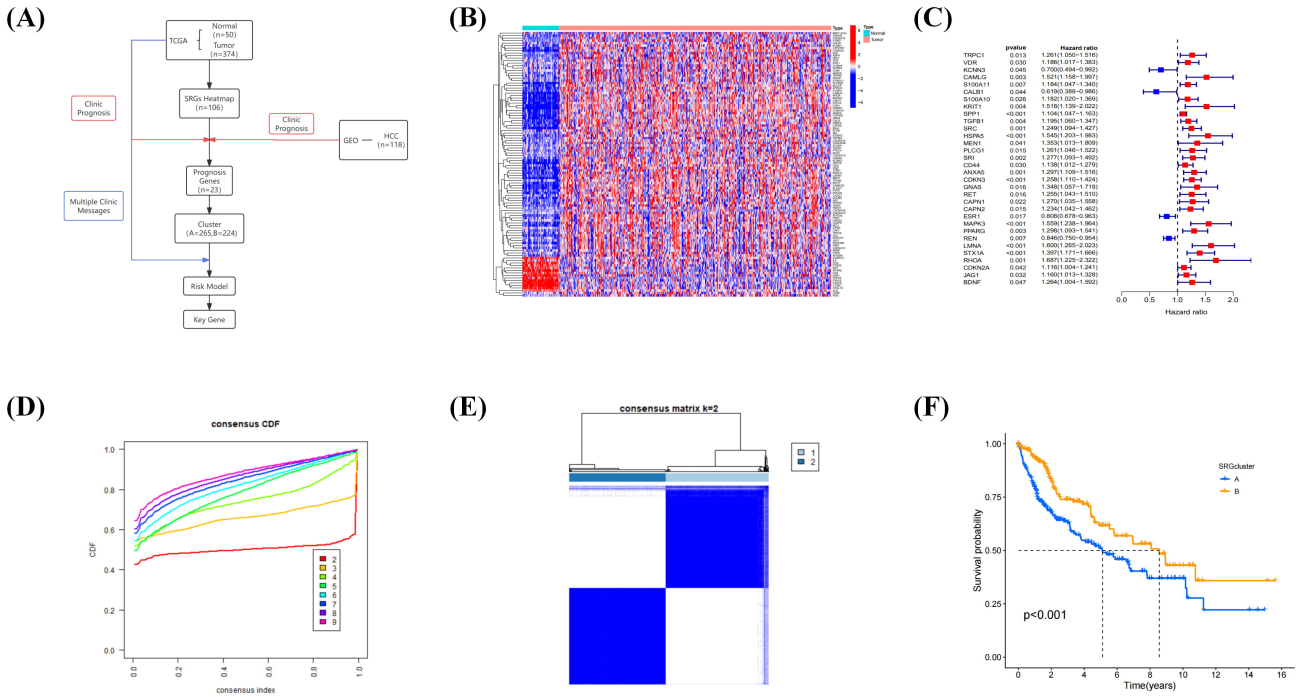

Fig. 2. DEG heatmap to illustrate prognostic genes. (A) Bioinformatics analysis workflow of this study. (B) Water blue represents normal sample tissues; pink represents tumor tissues; and red and blue in the DEG heatmap correspond to high and low gene expression, respectively. (C) Prognostic forest plot with color HRs: blue indicates genes with protective roles (HR <1); red indicates genes with risk roles (HR >1). (D) The consensus CDF plot showed optimal cluster stability at K = 2. (E) Cluster separation was most distinct at K = 2. (F) Kaplan–Meier curve showing that group B had significantly better OS than group A, with group B shown in orange and group A in blue. DEG, differentially expressed gene; HRs, hazard ratios; CDF, cumulative distribution function; OS, overall survival.

(4–5%, inhalation) and euthanized by cervical dislocation. Death was confirmed by cessation of respiration and heartbeat. Tumors were subsequently excised and weighed for further analyses.

2.21 Histopathological Analysis

Tumor and adjacent tissue specimens were fixed in 4% polyoxymethylene (G1101; Servicebio) at 37 °C with gentle agitation overnight. Following fixation, tissues were dehydrated, paraffin-embedded, and cut into sections with a thickness of 4–5 µm. Histological evaluation was carried out by hematoxylin and eosin (H&E) staining using a commercial H&E staining kit (G1076; Servicebio) in accordance with the manufacturer's instructions.

Immunohistochemical staining was performed on paraffin sections following deparaffinization and antigen retrieval. To reduce nonspecific binding, sections were blocked in 10% bovine serum albumin at 37 °C for 1 h. Slides were subsequently incubated with primary antibodies at 4 °C overnight and then treated with the corresponding HRP-conjugated secondary antibodies for 30 min at 37 °C. Signal development was carried out using the GTvision IHC detection system (Gene Tech Company Ltd., Shanghai, China) in accordance with the manufacturer's protocol, with PBS washes performed between steps.

2.22 Statistical Analyses

Statistical analyses were conducted using Origin 2022, ImageJ, and R Studio. Quantitative data obtained from qPCR and Western blot analyses are expressed as the mean ± standard deviation. Differences between the two groups were evaluated using a two-tailed Student's *t*-test, whereas one-way analysis of variance was applied for comparisons involving more than two groups. Statistical significance was defined as $p < 0.05$.

3. Results

3.1 DEGs With Prognosis Value

The bioinformatics analysis workflow of this study is summarized in Fig. 2A. To explore the involvement of SRGs in HCC, we compared their expression profiles between tumor and adjacent normal tissues. Among the 106 differentially expressed SRGs (FDR <0.05, |logFC| >1), 92 were upregulated in tumor samples, and 14 were downregulated (Fig. 2B). To assess the prognostic relevance of these genes, univariate Cox regression analysis was conducted. The resulting forest plot (Fig. 2C) highlighted 32 genes significantly correlated with OS in patients with HCC, which were subsequently selected for model construction. Of these, 28 genes functioned as risk factors (HR >1). Then, consensus clustering analysis was conducted to

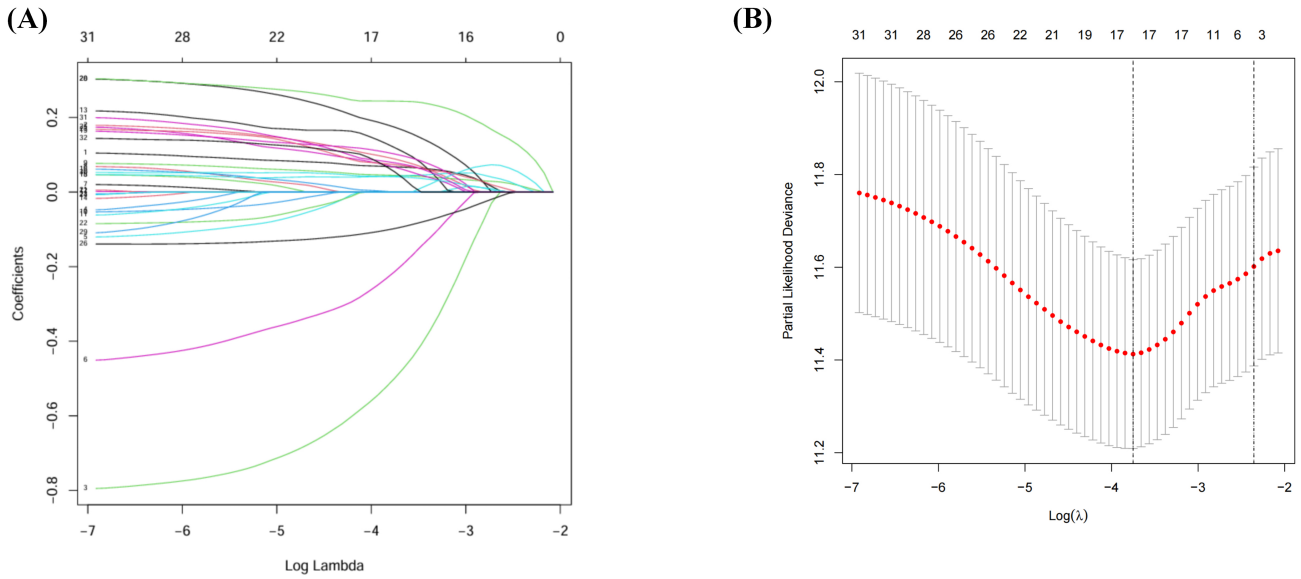

Fig. 3. Identification of risk signature. (A) LASSO regression of the OS-related genes. (B) Cross-validation for tuning the parameter selection in the LASSO regression. LASSO, least absolute shrinkage and selection operator.

further validate the prognostic impact of these genes. The CDF curve, evaluated for K = 2 to K = 9, indicated that K = 2 was the optimal number to define two distinct subgroups (Fig. 2D). The consensus matrix at K = 2 confirmed clear separation between the two clusters with high consensus, which demonstrated clear segregation between the two clusters (Fig. 2E). The clinical relevance of these two gene clusters was assessed using Kaplan–Meier survival analysis, which revealed a significant difference in OS between the clusters ($p < 0.001$). Patients in Cluster B exhibited a more favorable prognosis than those in Cluster A (Fig. 2F).

In summary, differential expression and univariate Cox regression analyses identified a subset of SRGs associated with HCC prognosis, including 28 risk genes. Consensus clustering based on these prognostic SRGs divided patients into two distinct subgroups with significantly different OS, indicating that these gene clusters may serve as robust indicators of clinical outcomes in HCC.

3.2 Identification of a 17-Gene Signature

To optimize the gene set, minimize overfitting, and select the most informative prognostic markers, we applied the LASSO regression. Based on the optimal penalty parameter (λ) determined by the minimum criteria, a 17-gene prognostic signature was established (Fig. 3A,B). The individual risk scores for patients were calculated using a formula combining the LASSO coefficients with the expression levels of these 17 genes.

In summary, LASSO regression enabled the identification of a concise 17-gene signature, and the derived risk scores provide a quantitative measure of patient prognosis in HCC.

3.3 Validation of the Risk Signature

To evaluate the prognostic value of the refined SRG signature, a risk score was calculated for each patient in the TCGA and GEO cohorts. Patients were stratified into low- and high-risk groups based on the median risk score. Kaplan–Meier analysis revealed a significant difference in OS, with patients in the low-risk group exhibiting markedly longer survival times than those in the high-risk group ($p < 0.001$; Fig. 4A). To assess the robustness of the prognostic model, the cohort was randomly split into a training set and testing set. In the training cohort, survival analysis revealed a significantly better outcome for patients classified as low risk ($p < 0.001$; Fig. 4B). The predictive performance of the risk score was further evaluated using time-dependent ROC analysis. In the whole cohort, the AUC for predicting OS was 0.755 at 1 year, 0.692 at 3 years, and 0.723 at 5 years (Fig. 4C). Similarly, in the training set, the AUC values were 0.821, 0.720, and 0.749 for 1-, 3-, and 5-year survival, respectively (Fig. 4D).

Overall, the SOCE-related prognostic signature successfully categorized patients into distinct risk groups that exhibited significant differences in clinical outcomes.

3.4 Refinement of the Prognostic Signature and Construction of a Nomogram

Multivariate Cox regression analysis was conducted to identify which genes within the 17-gene LASSO-derived prognostic signature had independent prognostic significance. This analysis identified nine genes as factors with independent prognostic value. A heatmap illustrating the expression patterns of these nine genes was created to visualize their relationship with patient outcomes (Fig. 5A).

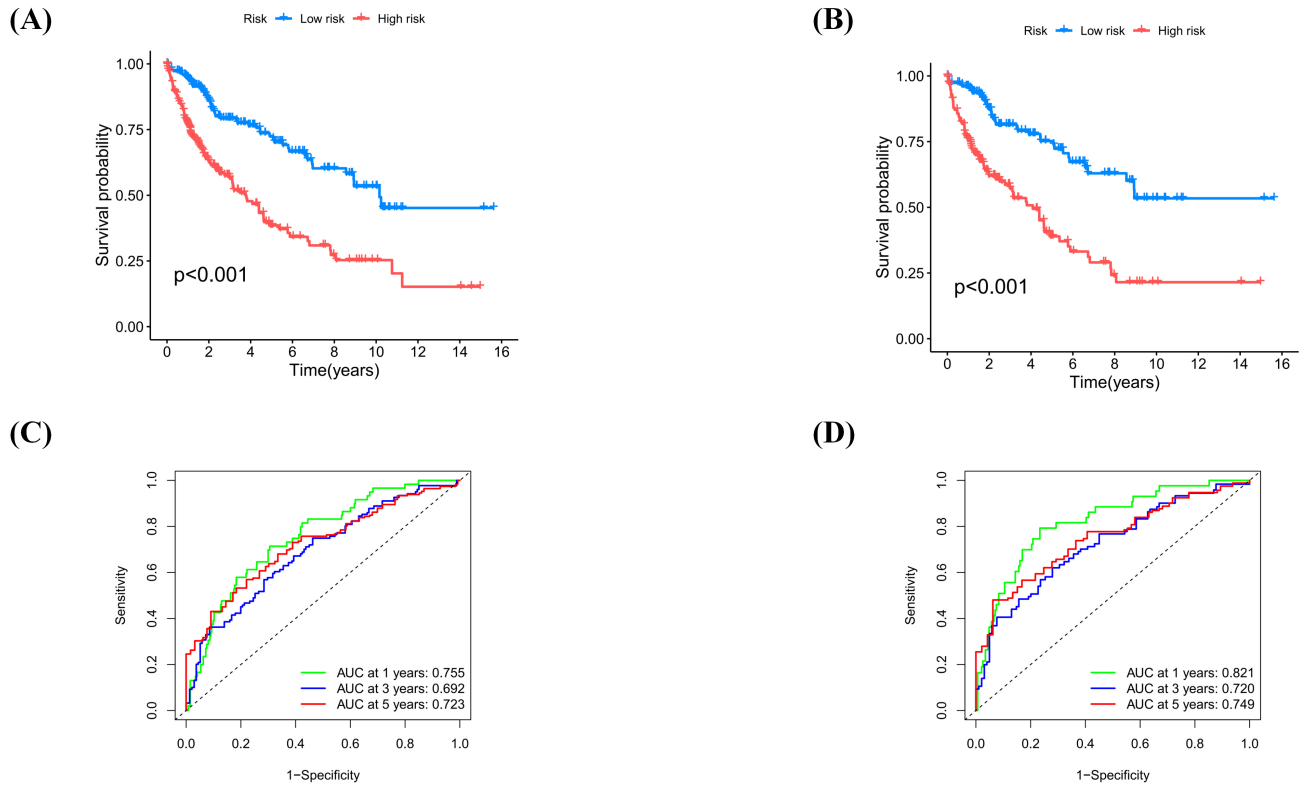

Fig. 4. Validation of risk signature in TCGA and GEO cohort. (A) Kaplan–Meier curves for the entire cohort show blue (low-risk) and red (high-risk) groups ($p < 0.001$). (B) Kaplan–Meier curves for the training group use the same label color as in (A) ($p < 0.001$). (C) ROC curve of the full cohort depicts 1-year survival in green, 3-year survival in blue, and 5-year survival in red. (D) In the training cohort ROC curve, the label color is the same as in (C) ($p < 0.001$). TCGA, The Cancer Genome Atlas; GEO, Gene Expression Omnibus; ROC, receiver operating characteristic.

Subsequently, the relationship between these nine genes and key clinicopathological factors was evaluated using multivariate analysis, and the results were visualized as a forest plot (Fig. 5B). The analysis revealed significant correlations between these genes and tumor T stage and N stage ($p < 0.001$ and $p < 0.05$, respectively), suggesting a potential role in local tumor invasion and progression. No statistically significant associations were observed with age or sex ($p > 0.05$). Age was retained in the subsequent model to reflect its established clinical relevance to cancer incidence, whereas sex was excluded due to lack of statistical significance, resulting in a more concise predictive tool.

By integrating the remaining variables, an individualized prognostic nomogram was generated to predict 1-, 3-, and 5-year OS probabilities (Fig. 5C). Curve analysis demonstrated strong concordance between the model's predicted and actual survival outcomes (Fig. 5D). Closer examination of the heatmap focused on risk-associated genes, and found that six (rearranged during transfection [RET], secreted phosphoprotein 1/osteopontin [SPP1], vitamin D receptor [VDR], annexin A5 [ANXA5], menin 1 [MEN1], and GNAS complex locus [GNAS]) were upregulated in the high-risk group, marking them as candidates for further analysis.

In summary, multivariate Cox regression identified nine genes with independent prognostic value, and their expression patterns were associated with key clinicopathological features such as tumor T and N stages. An individualized nomogram incorporating these variables reliably predicted 1-, 3-, and 5-year OS, with calibration curves confirming strong agreement between predicted and observed outcomes. Among the risk-associated genes, six (RET, SPP1, VDR, ANXA5, MEN1, and GNAS) were notably upregulated in the high-risk group, highlighting their potential relevance in HCC progression and patient prognosis.

3.5 Key Gene Filtration

To systematically investigate the enrichment patterns of the aforementioned six high-risk genes within the tumor immune microenvironment, we conducted a detailed analysis of each gene using the TISCH2 database, with representative results illustrated using the HCC dataset LIHC-GSE140228 (Fig. 6A). The analysis revealed that the key gene ANXA5 is highly expressed across multiple immune cell types, with notable enrichment particularly in dendritic cells and macrophages (Fig. 6B,C), suggesting its potential involvement in antigen presentation and innate immune regulation. In contrast, the other five genes showed gen-

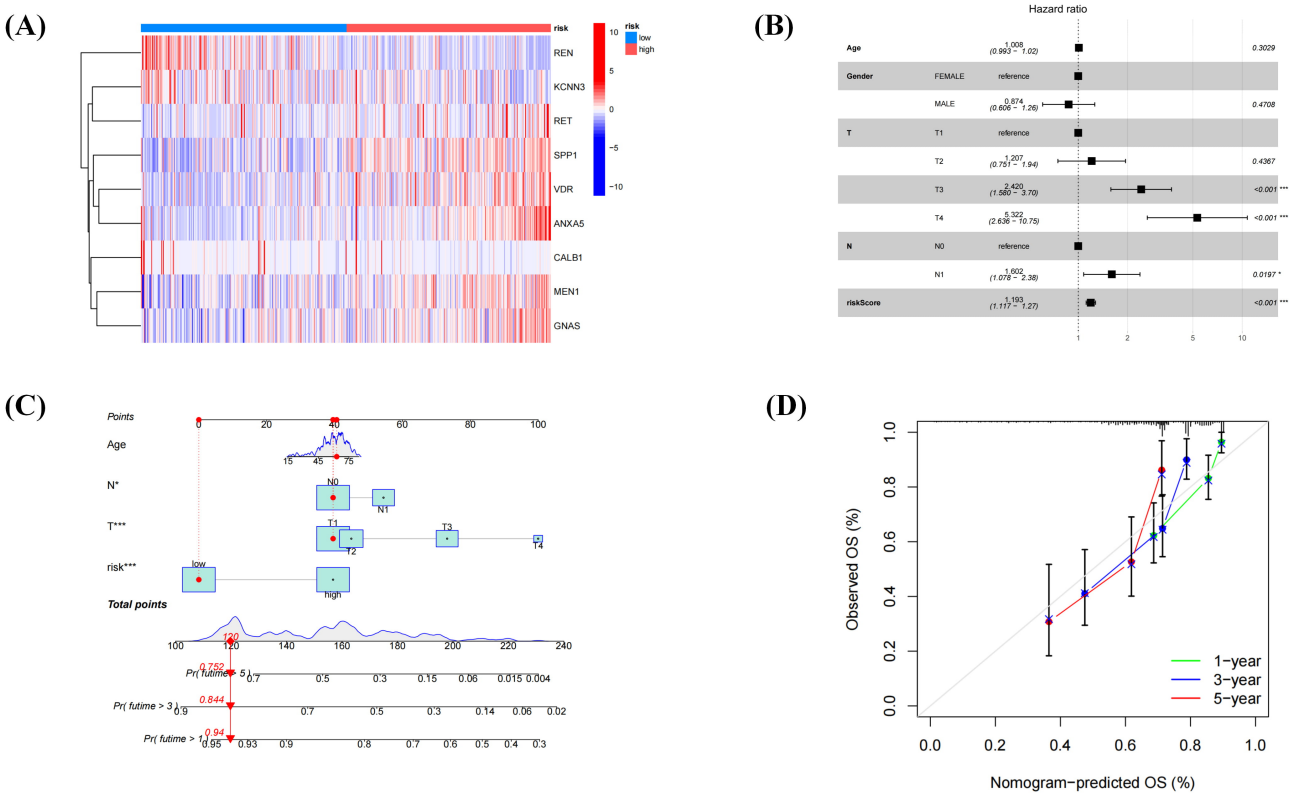

Fig. 5. Refinement of the prognostic signature and construction of a nomogram. (A) The risk heatmap shows nine genes. (B) Forest plot illustrating independent prognostic factors. (C) The nomogram incorporates four risk factors: age, T stage, N stage, and risk score. A specific point value is assigned to each factor on its corresponding scale. The total points are the sum of all four factors. A vertical line drawn from the total points axis to the outcome axes provides approximate predictions of the patient's 1-, 3-, and 5-year OS probabilities, as illustrated by the red vertical line in the figure. (D) The calibration curve of the nomogram shows that the green, blue, and red lines represent 1-, 3-, and 5-year survival probability calibrations, respectively.

erally low expression levels across various immune cells without significant enrichment. Although GNAS exhibited relatively high expression in certain cell populations, its expression pattern lacked cell type specificity and appeared diffuse, and thus was not pursued further. Based on these findings and established evidence linking ANXA5 to tumor progression, metastasis, and poor clinical outcomes in diverse cancers—including HCC—we selected it as a key gene for subsequent mechanistic investigation. Studies have shown that overexpressed ANXA5 in HCC is linked to malignant phenotypes and poor prognoses in *in vitro* and *in vivo* models [14,43–45]. Furthermore, high ANXA5 expression is significantly correlated with aggressive clinicopathological features and poor survival in various solid tumors [46–49]. To further elucidate the biological functions and regulatory networks of ANXA5, we constructed a protein–protein interaction network. Our analysis demonstrated a high-confidence interaction between ANXA5 and GAPDH (Fig. 6D), indicating their potential synergy in cellular metabolic regulation and immune responses. This finding provides a critical molecular clue for future functional studies.

In summary, while ANXA5 expression was detected in immune cell subsets within the tumor microenvironment—a topic for future research—this study primarily focused on investigating its functional role in key HCC malignant phenotypes, including proliferation, invasion, and metastatic potential.

3.6 Western Blotting and qPCR Analysis of ANXA5 and GAPDH Expression

To assess transfection efficiency, ANXA5 expression was evaluated in WT, NC, and three ANXA5-targeting shRNA groups (shRNA-ANXA5(h)-1, shRNA-ANXA5(h)-2, shRNA-ANXA5(h)-3) using Western blotting and qPCR. The results demonstrated that shRNA-ANXA5(h)-1 was the most effective sequence for KD (Fig. 7A–C), whereas no significant difference was observed between the WT and NC groups ($p > 0.05$). Consequently, we renamed shRNA-NC and shRNA-ANXA5(h)-1 to NC and ANXA5-KD, respectively, for simplicity.

Western blotting and qPCR analyses across WT, NC, and ANXA5-KD groups consistently demonstrated that ANXA5 KD did not significantly alter GAPDH expression levels ($p > 0.05$; Fig. 7D–F).

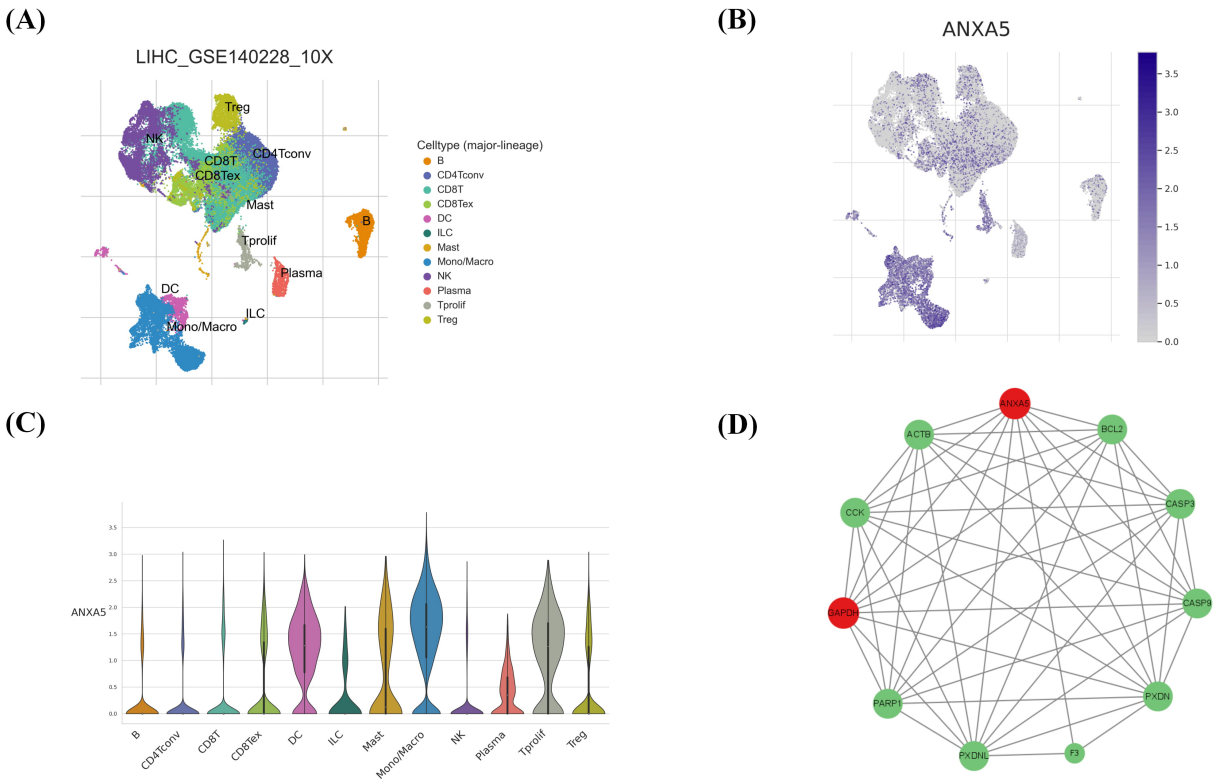

Fig. 6. Immune cell distribution map in LIHC-GSE140228. (A) Example of an immune cell distribution map; different colors represent different immune cells. (B) The map shows the distribution of the key gene ANXA5, with color intensity representing the degree of enrichment. (C) Immune cell expression of the key gene ANXA5, with column height representing enrichment degree. (D) The protein–protein interaction network demonstrated a strong interaction between ANXA5 and GAPDH. Node size represents the number of interactions, with larger nodes indicating greater connectivity. Since most proteins (except F3) had similar interaction counts, size differences were minimal. The most connected nodes, ANXA5 and GAPDH, are marked in red. Panels (A–C) were generated using the TISCH2 database (https://tisch.compbio.cn/gallery/). Panel (D) was constructed based on data obtained from the STRING database (version 12.0; https://cn.string-db.org/) and visualized using Cytoscape (v3.9.0).

3.7 Co-IP Analysis of ANXA5 and GAPDH Interaction

To determine whether the interaction between ANXA5 and GAPDH depends on ANXA5 expression levels, co-IP assays were conducted in WT, NC, and ANXA5-KD cells. Input analysis confirmed comparable GAPDH expression levels across all groups, whereas ANXA5-KD cells exhibited a significant reduction in ANXA5 levels. Co-IP using an anti-ANXA5 antibody followed by immunoblotting for GAPDH revealed a notable ANXA5–GAPDH interaction in WT and NC cells, which was substantially diminished in the ANXA5-KD group. No GAPDH signal was detected in the IgG control IP (Fig. 8A). Quantitative analysis of input samples showed no significant differences in GAPDH expression among the groups ($p > 0.05$), whereas ANXA5 levels were significantly reduced in the ANXA5-KD group ($p < 0.05$; Fig. 8B). Quantitative analysis of IP'd samples revealed a significant difference in GAPDH levels between the ANXA5-KD group and both the WT and NC groups ($p < 0.05$), with no detectable GAPDH signal in the IgG control group (Fig. 8C).

In summary, these findings indicate that ANXA5 forms a specific complex with GAPDH in HCC cells in an ANXA5-dependent manner. Importantly, ANXA5 depletion markedly weakened the ANXA5–GAPDH interaction without altering total GAPDH protein levels, suggesting that ANXA5 regulates GAPDH primarily via protein–protein interaction rather than expression control. This observation provides a mechanistic basis for subsequent analyses exploring how ANXA5 modulates GAPDH enzymatic activity and downstream metabolic and Ca^{2+} signaling pathways.

3.8 ANXA5 Regulates HCC Cell Proliferation, Migration, and Apoptosis In Vitro

To systematically investigate the role of ANXA5 in the malignant behavior of HCC cells, functional assays including wound healing, CCK-8 proliferation, and flow cytometry-based apoptosis analysis were performed.

In the wound healing assay, ANXA5-KD cells exhibited significantly slower wound closure compared with WT and NC cells (Fig. 9A). Quantitative analysis confirmed a

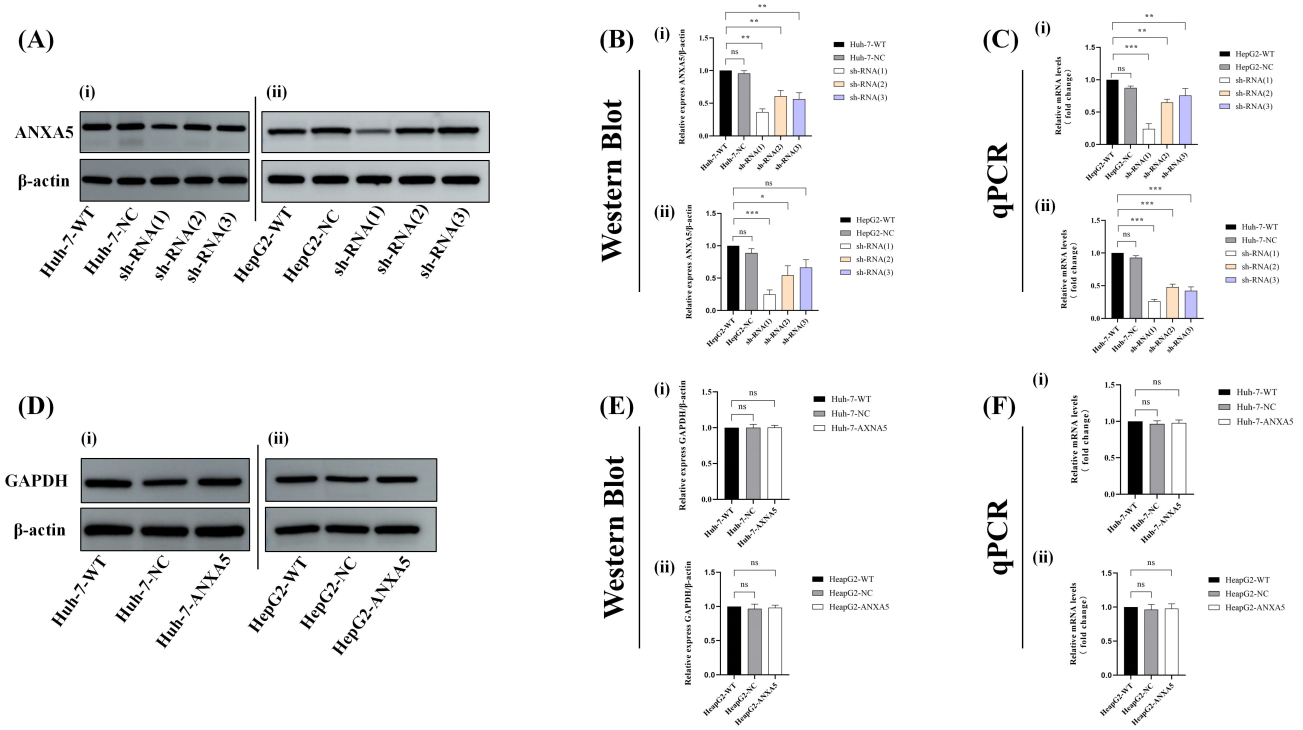

Fig. 7. Western blotting and qPCR analysis of ANXA5 and GAPDH expression. (A) Western blot bands of ANXA5. (B) Quantitative analysis of ANXA5 protein expression based on Western blot band intensity ($p < 0.05$). (C) Relative mRNA expression level of ANXA5 measured by qPCR ($p < 0.05$). (D) Western blot bands of GAPDH. (E) Quantitative analysis showing no significant difference in GAPDH protein expression among groups ($p > 0.05$). (F) Relative mRNA expression level of GAPDH measured by qPCR, with no statistically significant differences between groups ($p > 0.05$). (i) Huh-7, (ii) HepG2. Statistical significance is indicated as follows: *, $p < 0.05$; **, $p < 0.01$; ***, $p < 0.001$; ns, not significant. Western blot bands were imaged using a chemiluminescence imaging system (SCG-W3000, Servicebio, Wuhan, China). Quantitative bar graphs were generated using GraphPad Prism 10.

marked reduction in cell migration rate in the KD group ($p < 0.05$; Fig. 9B), indicating that ANXA5 depletion effectively inhibited HCC cell motility.

Cell proliferation was assessed using the CCK-8 assay, which showed that absorbance values in the ANXA5-KD group showed significantly decreased levels relative to the control groups ($p < 0.05$; Fig. 9C), suggesting substantially suppressed proliferative activity and highlighting the role of ANXA5 in maintaining HCC cell proliferation.

Flow cytometry with Annexin V-FITC/PI staining was used to measure the apoptosis level. Scatter plots revealed a notable increase in the proportions of apoptotic cells in the ANXA5-KD groups (Fig. 9D). Quantitative analysis confirmed that the proportion of apoptotic cells was markedly increased in the KD group relative to the control groups ($p < 0.05$; Fig. 9E), indicating a pronounced pro-apoptotic effect of ANXA5 KD.

Together, these findings establish that ANXA5 plays a critical role in regulating migration, proliferation, and apoptosis in HCC cells. ANXA5 KD led to reduced cell migration and growth while significantly increasing apoptosis, highlighting its potential as a therapeutic target for HCC.

3.9 ANXA5 Modulates Ca^{2+} Signaling Through the GAPDH/IP_3 Pathway

Based on prior evidence indicating a strong interaction between ANXA5 and GAPDH, and having confirmed that ANXA5 does not alter GAPDH expression, we investigated whether ANXA5 influences GAPDH enzymatic activity. An ELISA-based assay revealed a positive correlation between ANXA5 levels and GAPDH activity ($p < 0.05$; Fig. 10A).

To investigate the potential mechanism, we examined whether ANXA5 may influence PIP_2 metabolism through GAPDH enzymatic activity. Since direct quantification of PIP_2 was technically challenging, we measured the levels of its downstream metabolite, IP_3, as an indirect indicator of PIP_2 hydrolysis. ELISA analysis showed a significant decrease in IP_3 concentration following ANXA5 knockdown ($p < 0.05$; Fig. 10B).

To investigate whether ANXA5 regulates intracellular IP_3 levels via the PLC pathway, we performed pharmacological inhibition and genetic KD experiments. Cells were divided into four groups: vehicle control, ANXA5-KD, U73122, and U73343 (Fig. 10C). Measurement of intracellular IP_3 revealed that U73122 treatment and ANXA5-KD

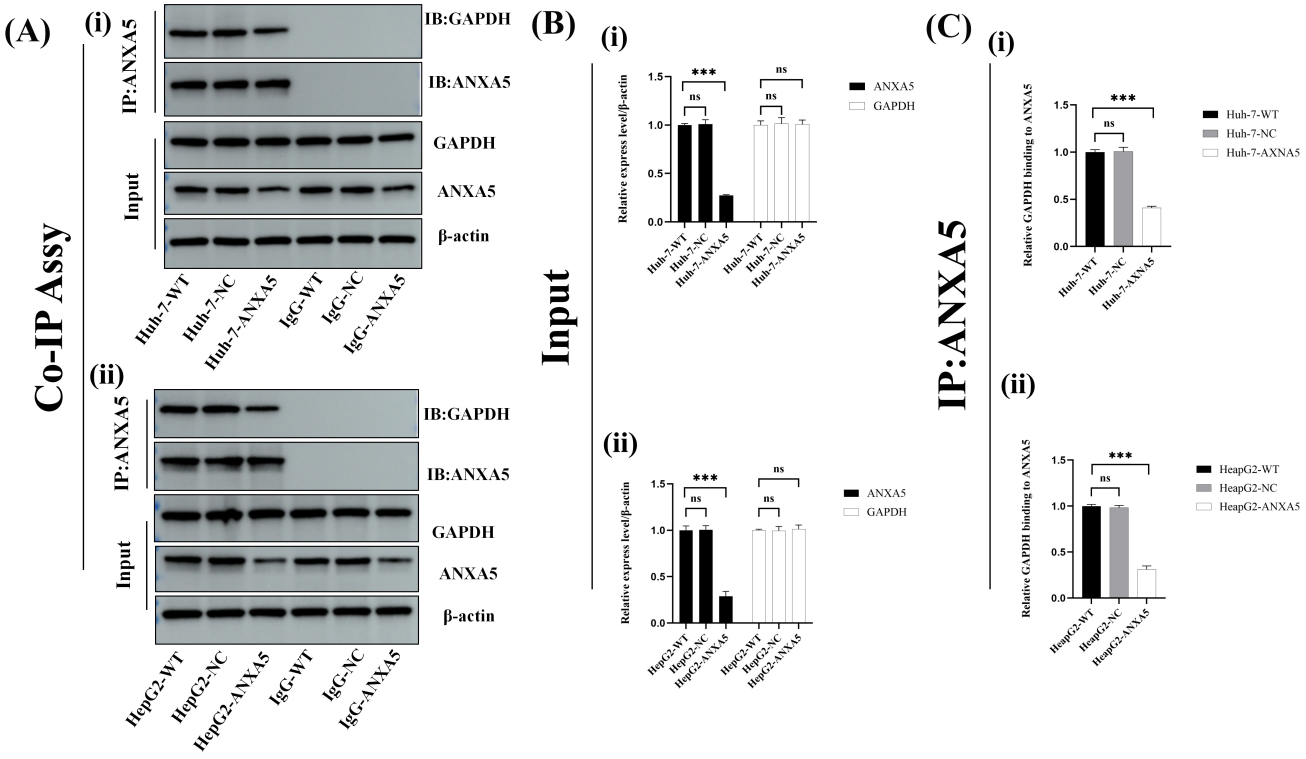

Fig. 8. Interaction of ANXA5 with GAPDH by Co-IP. (A) Input bands showed comparable GAPDH expression across all groups, whereas ANXA5 expression was markedly reduced in ANXA5-KD cells. IP with an anti-ANXA5 antibody followed by immunoblotting for GAPDH revealed a strong ANXA5–GAPDH interaction in WT and NC cells, which was substantially diminished upon ANXA5-KD, whereas no GAPDH signal was detected in the IgG IP control. (B) Quantitative analysis showed no significant difference in GAPDH protein expression among input sample groups ($p > 0.05$), whereas there was a significant difference in ANXA5 protein expression in the ANXA5-KD group ($p < 0.05$). (C) Quantitative analysis of the ANXA5-KD group showed significant differences in GAPDH signals among IP-ANXA5 groups ($p < 0.05$), with no signal detected in the IP-IgG control. (i) Huh-7, (ii) HepG2. Co-IP, Co-immunoprecipitation; KD, knockdown; WT, wild-type. Statistical significance is indicated as follows: ***, $p < 0.001$; ns, not significant. Co-IP bands were imaged using a chemiluminescence imaging system (SCG-W3000, Servicebio, Wuhan, China). Quantitative bar graphs were generated using GraphPad Prism 10.

both significantly reduced IP_3 levels compared with vehicle control ($p < 0.05$), whereas U73343 had no significant effect ($p > 0.05$). Notably, U73122 exhibited the strongest inhibition of IP_3 production, consistent with its role as a PLC inhibitor. These results indicate that ANXA5 contributes to IP_3 generation in HCC cells, likely via the PLC pathway, and that pharmacological PLC inhibition mimics the effect of ANXA5 depletion, supporting the proposed ANXA5/GAPDH/IP_3/SOCE working model.

To further examine the functional impact, cytosolic Ca^{2+} dynamics were assessed using a fluorescent Ca^{2+} indicator in Huh-7 and HepG2 cells with ANXA5-KD. Ca^{2+} oscillation curves showed that ANXA5-KD attenuated both ER Ca^{2+} release and the SOCE peak compared with WT and NC groups (Fig. 10D). The AUC for ER release and SOCE peak was quantified from the Ca^{2+} oscillation curves (Fig. 10E), confirming that decreased ANXA5 expression compromised ER Ca^{2+} release and consequently diminished SOCE ($p < 0.05$).

In summary, our findings suggest that ANXA5 may positively influence GAPDH enzymatic activity without affecting its expression levels. Moreover, ANXA5 knockdown was associated with a marked reduction in the downstream metabolite IP_3, which may reflect indirect alterations in PIP_2 metabolism. Pharmacological inhibition of PLC with U73122 mimicked the effects of ANXA5 depletion, supporting the involvement of the PLC pathway in ANXA5-mediated IP_3 generation. Functionally, ANXA5 deficiency impaired intracellular Ca^{2+} signaling, as evidenced by diminished ER Ca^{2+} release and reduced SOCE in Huh-7 and HepG2 cells. Collectively, these results suggest that ANXA5 regulates HCC cell Ca^{2+} dynamics through GAPDH-dependent modulation of the PLC/IP_3 axis, consistent with the proposed ANXA5/GAPDH/IP_3/SOCE working model.

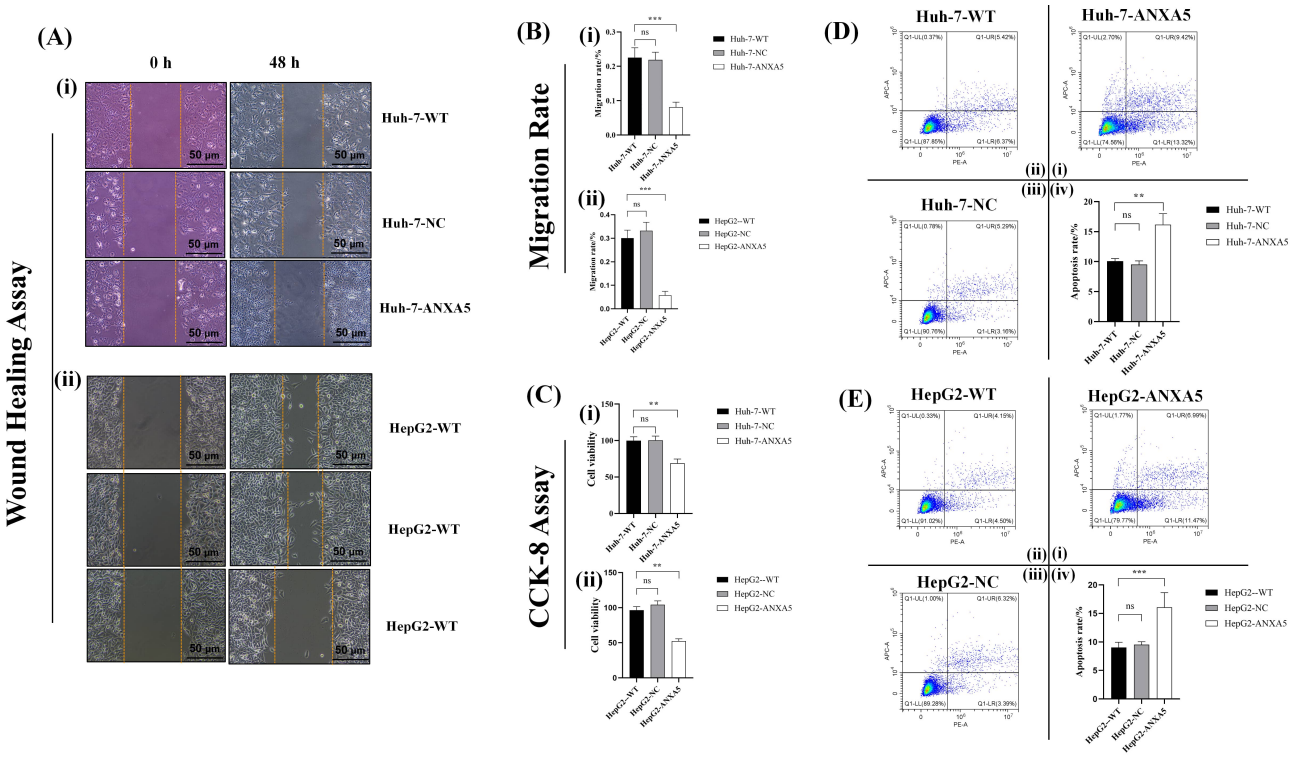

Fig. 9. ANXA5 regulates HCC cells *in vitro*. (A) Micrographs of wound healing assays: (i) Huh-7, (ii) HepG2. (B) Quantification of cell migration in the wound healing assay: (i) Huh-7, (ii) HepG2. (C) CCK-8 assay quantifying cell proliferation: (i) Huh-7, (ii) HepG2. (D) Flow cytometry scatter plots of apoptosis detection. The quadrants represent: lower left (viable cells), upper left (mechanically damaged cells), upper right (late apoptotic cells), and lower right (early apoptotic cells); (i) Quantitative analysis of Huh-7-WT, (ii) Huh-7-NC, (iii) Huh-7-ANXA5, (iv) Huh-7 cells. (E) Flow cytometry scatter plots of apoptosis detection. (i) Quantitative analysis of HepG2-WT, (ii) HepG2-NC, (iii) HepG2-ANXA5, (iv) HepG2 cells. Statistical significance is indicated as follows: **, $p < 0.01$; ***, $p < 0.001$; ns, not significant. Scale bar = 50 μm. Wound healing images were captured using a microscope (model: XSP-C204), and apoptosis data were analyzed using FlowJo (v10.8.1). Quantitative bar graphs were generated using GraphPad Prism 10.

3.10 ANXA5 Promotes Tumor Growth and Malignancy In Vivo

To evaluate the *in vivo* function of ANXA5, nude mice were subcutaneously inoculated with WT, NC, or ANXA5-KD cells (Huh-7) in the right flank. Measurement of resected tumors showed that knocking down ANXA5 significantly reduced tumor volumes compared to the WT and NC groups (Fig. 11A,B). Quantitative analysis further demonstrated that ANXA5 KD markedly reduced the rate of tumor progression (Fig. 11C) and tumor burden at sacrifice (Fig. 11D), and was associated with a slower decline in mouse body weight (Fig. 11E), suggesting a less aggressive tumor burden.

Histological examination using H&E staining showed that tumors from the control groups exhibited more compact and dense architecture compared with the more loosened structure observed in ANXA5-KD tumors (Fig. 11F). Immunohistochemical analysis of Ki-67, a proliferation marker, and vimentin, a marker of epithelial–mesenchymal transition (EMT), revealed substantially higher expression levels in the WT and NC groups than in the ANXA5-KD group. Additionally, staining for the M2 macrophage marker CD206 showed denser positive signals in control tumors. These findings suggest a potential association between ANXA5 expression and M2 macrophage–related signals within the tumor microenvironment (Fig. 11F). Quantitative analysis of staining intensity confirmed significant reductions in proliferation, malignancy, and M2 marker expression upon ANXA5 KD ($p < 0.05$; Fig. 11G–I). Collectively, these findings indicate that ANXA5 contributes to tumor growth, malignancy, and the M2-polarized tumor microenvironment *in vivo*.

In summary, the *in vivo* experiments demonstrated that ANXA5 depletion significantly suppressed tumor growth and progression. Tumors derived from ANXA5-KD cells exhibited smaller volumes, slower growth kinetics, and reduced tumor burden at the endpoint compared with WT and NC controls. Histological assessment revealed a less compact tumor architecture in ANXA5-KD tumors, accompanied by decreased Ki-67 and vimentin expression, indicating diminished proliferation and EMT activity. Furthermore, reduced CD206 staining suggested a decrease in M2-associated macrophage signals within the tumor tissue. Taken together, these findings indicate that

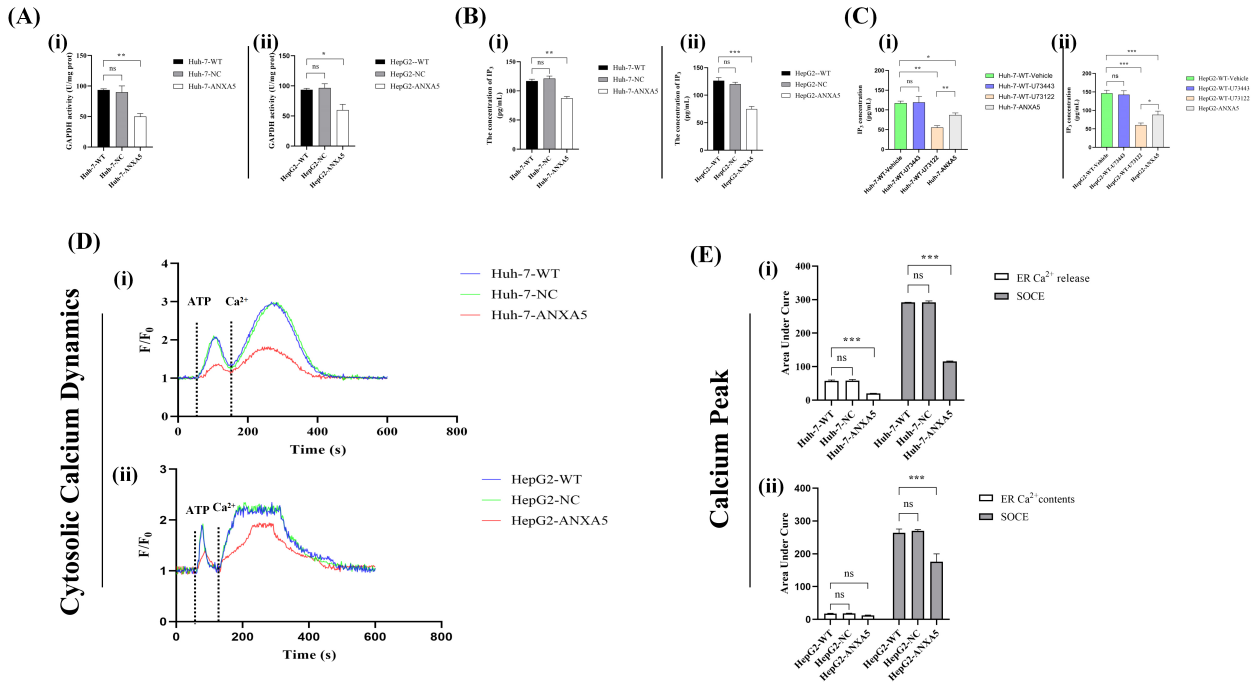

Fig. 10. ANXA5 modulates Ca^{2+} signaling through the GAPDH/IP_3 pathway. (A) GAPDH enzyme activity was determined by spectrophotometrically monitoring the rate of NADH consumption during the reaction. (B) Measurement of IP_3 level. (C) IP_3 rescue experiment. There were no significant differences between the vehicle and U73443 groups ($p > 0.05$), unlike the comparison between the ANXA5-KD and U73122 groups ($p < 0.05$). The rescue assay shows that U73122 (a PLC inhibitor) and ANXA5-KD similarly impair IP_3 production. (D) In the Ca^{2+} oscillation curve, the first peak represents ER Ca^{2+} release, whereas the second peak corresponds to the SOCE. The first dashed line indicates the time point of ATP stimulation, and the second dashed line marks the addition of extracellular Ca^{2+}. (E) AUC of ER Ca^{2+} release and SOCE peak. (i) Huh-7, (ii) HepG2. IP_3, inositol 1,4,5-trisphosphate; PLC, phospholipase C; AUC, area under the curve. Statistical significance is indicated as follows: *, $p < 0.05$; **, $p < 0.01$; ***, $p < 0.001$; ns, not significant. This panel was generated using GraphPad Prism 10.

ANXA5 expression is associated with tumor growth, malignant phenotypes, and changes in immune-related markers *in vivo*.

4. Discussion

The development and progression of HCC involves a complex interplay of diverse biological and environmental factors, including genetic alterations, viral infections, and aflatoxin exposure, among others.

Tumor metastasis and postoperative recurrence are widely acknowledged as key determinants of unfavorable outcomes in patients with HCC. HCC therefore remains a formidable global health challenge due to its strong propensity for recurrence and metastasis [50–55].

We identified a working model in which ANXA5 drives HCC progression through functional engagement of the SOCE signaling pathway. Our findings suggest a potential association between ANXA5-related changes in GAPDH activity and alterations in PPI metabolism, including PIP_2. Although PIP_2 was not directly quantified, the observed changes in downstream signaling are consistent with indirect modulation of PPI hydrolysis. These alterations were accompanied by changes in SOCE-dependent Ca^{2+} influx, which may contribute to the regulation of malignant phenotypes of HCC cells, such as proliferation, migration, and survival.

The most significant and novel finding of our study was the identification of a functional link between ANXA5 and GAPDH. While GAPDH has long been recognized as a central mediator of the Warburg effect, a key metabolic reprogramming event in cancer, its regulation by annexin family proteins, particularly ANXA5, remained largely unexplored. Through integrated approaches including Western blotting, qPCR, ELISA, and co-IP, we provided initial evidence of a robust interaction between ANXA5 and GAPDH. Interestingly, while ANXA5 depletion did not affect GAPDH expression at either the transcriptional or protein level, it significantly reduced its enzymatic activity. Consistently, Co-IP assays revealed a physical association between ANXA5 and GAPDH, supporting the notion that ANXA5 modulates GAPDH function through protein–protein interaction rather than expression control. Together, these findings suggest that ANXA5 influences glycolysis and adds a metabolic regulatory layer by controlling GAPDH through post-translational mechanisms.

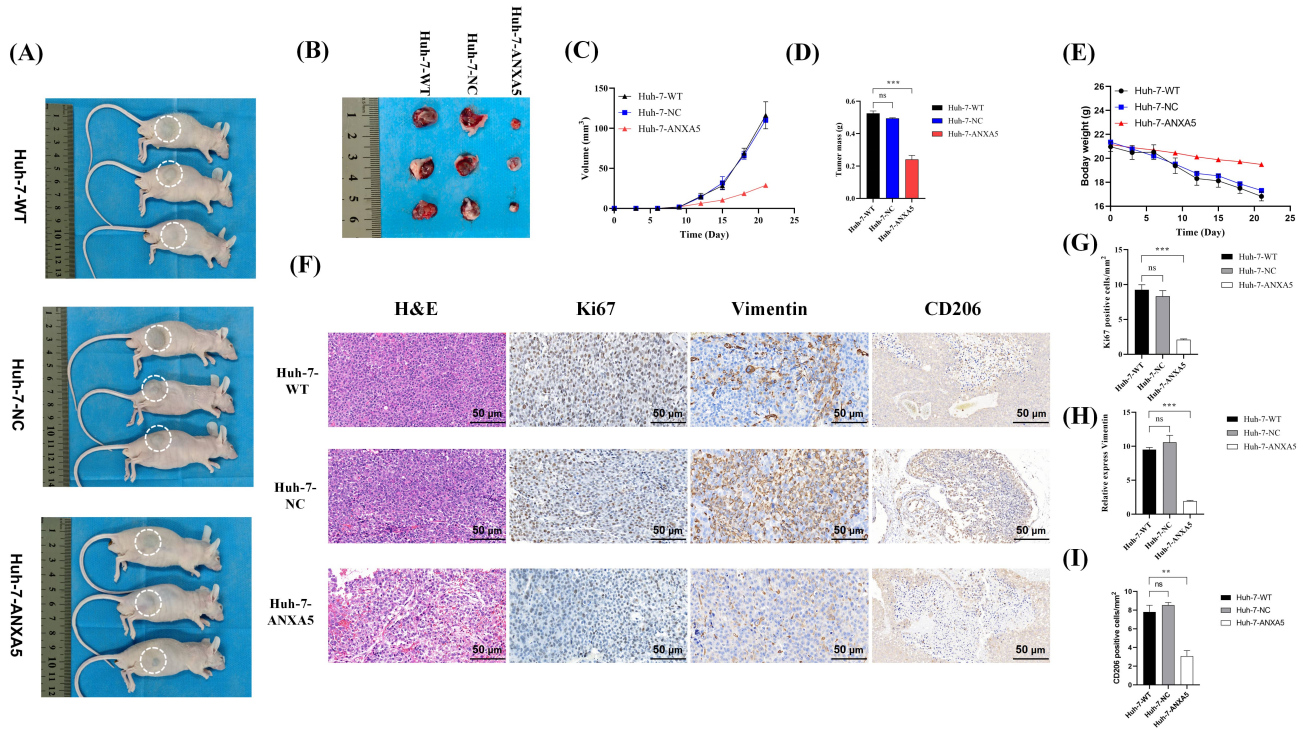

Fig. 11. ANXA5 promotes tumor growth and malignancy *in vivo*. (A) Images of tumors *in situ*. (B) Excised tumor specimens from each group. (C) Tumor growth curves over time. (D) Bar graph showing final tumor mass. (E) Body weight changes of mice during the study. (F) Histological, cross-sectional analysis (top to bottom respectively) of Huh-7-WT, Huh-7-NC, and Huh-7-ANXA5 cells; (left to right respectively) H&E staining of Ki-67, vimentin, and CD206. Scale bar = 50 μm. (G) Quantification of Ki-67-positive cells. (H) Quantification of vimentin expression. (I) Quantification of CD206-positive cells. H&E, hematoxylin and eosin. Statistical significance is indicated as follows: **, $p < 0.01$; ***, $p < 0.001$; ns, not significant. Line graphs and bar charts in this panel were generated using GraphPad Prism 10, and HE and IHC images were acquired using CaseViewer.

Given that PPI synthesis (including PIP_2) relies on GAPDH-dependent glycolytic pathways [33–36,56], the reduced IP_3 levels observed after ANXA5 KD likely stem from compromised GAPDH activity.

Our results indicate that ANXA5 positively regulates GAPDH enzymatic activity without altering its expression level. Depletion of ANXA5 led to a marked reduction in the downstream metabolite IP_3, suggesting a potential role for ANXA5 in PIP_2 metabolism. Pharmacological inhibition of PLC using U73122 recapitulated the effects of ANXA5 loss, supporting the involvement of the PLC pathway in ANXA5-mediated IP_3 generation. Collectively, these findings suggest that ANXA5 modulates Ca^{2+} dynamics in HCC cells through a GAPDH-dependent regulation of the PLC/IP_3 axis, consistent with the proposed ANXA5/GAPDH/IP_3/SOCE working model.

Taken together, our data suggest a potential signaling framework in which ANXA5 may be associated with enhanced GAPDH-related glycolytic activity, potentially influencing PPI metabolism, including PIP_2 [57]. Although PIP_2 was not directly measured, the observed changes in IP_3 levels are consistent with indirect modulation of PLC-dependent PIP_2 hydrolysis. These alterations were accompanied by changes in ER Ca^{2+} release and subsequent SOCE activation.

Moreover, through its interaction with PIPKIγ, ANXA5 may facilitate PIP_2 production and contribute to stabilizing ER–PM junctions, which are essential for SOCE channel assembly and function [25,26]. Thus, ANXA5 occupies a critical position at the intersection of metabolism and Ca^{2+} signaling, simultaneously regulating both the initiator (IP_3 production) and structural platform (PIP_2-enriched junctions) of SOCE. This dual role establishes a feed-forward mechanism that robustly sustains pro-tumorigenic Ca^{2+} signaling in HCC.

SOCE is the principal pathway for Ca^{2+} influx in non-excitable cells, including HCC cells [58–60]. Disruption of this pathway through ANXA5 KD produced profound phenotypic consequences, as evidenced by suppressed proliferation and migration, alongside increased apoptosis. The induction of apoptosis upon ANXA5 depletion revealed an additional dimension of its pro-tumorigenic function. Beyond its role in the GAPDH/IP_3/SOCE axis, we hypothesize that ANXA5 may directly enhance the expression of cell survival-promoting proteins such as B-cell lymphoma 2 (Bcl-2), a hypothesis supported by preliminary data.

This hypothesis is consistent with ANXA5's established ability to bind phosphatidylserine on the apoptotic cell surface, thereby masking "eat-me" signals and conferring a survival advantage [61,62]. Bcl-2, a well-characterized anti-apoptotic protein, promotes cell survival by directly targeting Bcl-2-associated X protein (BAX) and Bcl-2 homologous antagonist/killer (BAK) to antagonize their pro-apoptotic roles [62,63]. This interaction prevents BAX/BAK oligomerization, preserves mitochondrial membrane integrity, and suppresses the initiation of intrinsic apoptosis [64–66]. Thus, ANXA5 likely promotes HCC cell survival through a dual mechanism: first, by sustaining pro-survival Ca^{2+} signaling via SOCE; and second, by potentially upregulating anti-apoptotic proteins.

These mechanistic insights were strongly corroborated by our *in vivo* experiments. Significant reductions in tumor volume, weight, and expression of the proliferation marker Ki-67 and the mesenchymal marker vimentin upon ANXA5 KD, highlight its critical role in driving tumor growth and malignancy. Moreover, the attenuated decline in body weight among mice bearing ANXA5-deficient tumors suggested a reduced overall tumor burden, highlighting the therapeutic potential of targeting ANXA5 in HCC.

Our bioinformatic analyses suggested a potential immunomodulatory role for ANXA5 in shaping the tumor microenvironment. Numerous studies have reported that metabolic processes within the tumor microenvironment are extensively reprogrammed to support cancer cell survival and progression [67,68]. Cancer cells frequently shift toward the Warburg effect, a metabolic adaptation characterized by increased glucose uptake and elevated lactate production [69–71]. This reprogramming enables tumor cells to thrive under nutrient-limited and hypoxic conditions, thereby facilitating tumor progression [72].

Significant overrepresentation of ANXA5 was detected in dendritic cells and macrophages, two pivotal antigen-presenting cell populations that constitute the immune system's first line of defense [73]. This cellular distribution indicates that ANXA5 might interfere with the early steps of cancer cell recognition, potentially contributing to immune evasion. More intriguingly, our preliminary data suggest that ANXA5 expression may be associated with increased markers of M2-like macrophage polarization. Given that M2 macrophages are well-established mediators of immunosuppression, angiogenesis, and tumor-supportive tissue remodeling [74], this observation raises the possibility that ANXA5 could contribute to shaping an immunosuppressive tumor microenvironment.

Taken together, these findings support the hypothesis that ANXA5 may contribute to HCC progression not only through tumor-intrinsic mechanisms—namely the GAPDH/SOCE axis—but also through tumor-extrinsic pathways. ANXA5 expression was associated with increased markers of M2-like macrophages, suggesting a potential link to features of an immunosuppressive tumor microenvironment. These observations may correlate with reduced anti-tumor immune activity, which could contribute to tumor growth and survival, although direct functional validation is needed. Based on current literature and our experimental results [75–78], We preliminarily propose that ANXA5 expression may be associated with M2-like macrophage characteristics and may contribute to features of the tumor microenvironment, a hypothesis that will be further explored in future studies [79].

In conclusion, our work supports a model wherein the ANXA5/GAPDH/IP_3/SOCE pathway drives HCC progression by linking metabolic reprogramming with sustained oncogenic Ca^{2+} signaling. Moving beyond correlative observations, we established a definitive mechanistic cascade linking a membrane-associated protein (ANXA5) to a key glycolytic enzyme (GAPDH) and ultimately to a fundamental second-messenger system (Ca^{2+}).

Furthermore, our computational analyses suggest that ANXA5 expression may be associated with features of an immunosuppressive tumor microenvironment, potentially linked to M2-like macrophage characteristics. These multifaceted findings not only advance our understanding of HCC pathogenesis but also position ANXA5 as a promising therapeutic target.

Future research should focus on developing specific ANXA5 inhibitors to assess their impact on immune regulation and tumor microenvironment remodeling *in vivo*. In addition, exploring combination strategies that target this newly identified signaling axis alongside current standard therapies may ultimately offer innovative and more effective treatment options for this aggressive malignancy.

5. Limitations

This study has several limitations that should be acknowledged. First, although our findings suggest a potential mechanistic link between ANXA5, GAPDH activity, and the IP_3/SOCE signaling axis, the direct causal relationship and detailed molecular interactions remain to be further elucidated. Second, while both Huh-7 and HepG2 cell lines were used for in vitro validation, the in vivo experiments were conducted using only one cell line, which may limit the generalizability of the findings. Third, the regulatory effects of ANXA5 on phosphoinositide metabolism were inferred based on functional assays, and more direct evidence, such as lipidomics or metabolic flux analysis, is still needed. In addition, the sample size in animal experiments was relatively limited, and further studies with larger cohorts are required to strengthen the conclusions. Finally, the clinical relevance of the ANXA5/GAPDH/IP_3/SOCE axis warrants further validation in patient-derived samples and prospective studies.

6. Conclusions

ANXA5 may enhance HCC malignancy by promoting GAPDH activity, leading to increased IP_3 production and strengthened SOCE-mediated Ca^{2+} influx. Our results support a working model in which the ANXA5/GAPDH/IP_3/SOCE axis contributes to HCC progression, highlighting ANXA5 as a potential therapeutic target.

Availability of Data and Materials

The datasets used and analyzed during the current study are available from the corresponding author or first author upon reasonable request.

Author Contributions

XGZ, FYW: conceived and designed this study. WCG, XCZ, SM: conducted experiments and analyzed data. WCG, XCZ, SM: constructed animal models. WCG, SM: interpreted data. WCG: drafted the manuscript. XGZ, FYW: reviewed data and proofread manuscripts. All authors contributed to editorial changes in the manuscript. All authors read and approved the final manuscript. All authors have participated sufficiently in the work and agreed to be accountable for all aspects of the work.

Ethics Approval and Consent to Participate

All animal experiments were approved by the Animal Care and Use Committee of Bengbu Medical University (Approval No. [2025]514), and were conducted in accordance with the ARRIVE guidelines and the institutional guidelines for the care and use of laboratory animals.

Acknowledgment

The authors thank Graduate School, Bengbu Medical University, Anhui No. 2 Provincial People's Hospital and the Anhui Provincial Key Laboratory of Occupational Health for support.

Funding

This study was supported by the University Research Project Education Department of Anhui Province (2024AH050554), Research Innovation Plan Project for Postgraduates of Bengbu Medical University in the 2024 Academic Year (Byycx24084) and the Scientific Research Project of Anhui Provincial Healthcare Commission (AHWJ2022a003).

Conflict of Interest

The authors declare no conflict of interest.

References

[1] Sung H, Ferlay J, Siegel RL, Laversanne M, Soerjomataram I, Jemal A, *et al*. Global Cancer Statistics 2020: GLOBOCAN Estimates of Incidence and Mortality Worldwide for 36 Cancers in 185 Countries. CA: A Cancer Journal for Clinicians. 2021; 71: 209–249. https://doi.org/10.3322/caac.21660.

[2] Mejia JC, Pasko J. Primary Liver Cancers: Intrahepatic Cholangiocarcinoma and Hepatocellular Carcinoma. The Surgical Clinics of North America. 2020; 100: 535–549. https://doi.org/10.1016/j.suc.2020.02.013.

[3] Campbell K. Hepatitis B and the liver cancer endgame. Nature. 2022; 603: S64–S65. https://doi.org/10.1038/d41586-022-00821-0.

[4] Tan EY, Danpanichkul P, Yong JN, Yu Z, Tan DJH, Lim WH, *et al*. Liver cancer in 2021: Global Burden of Disease study. Journal of Hepatology. 2025; 82: 851–860. https://doi.org/10.1016/j.jhep.2024.10.031.

[5] Vogel A, Meyer T, Sapisochin G, Salem R, Saborowski A. Hepatocellular carcinoma. Lancet. 2022; 400: 1345–1362. https://doi.org/10.1016/S0140-6736(22)01200-4.

[6] Brown ZJ, Tsilimigras DI, Ruff SM, Mohseni A, Kamel IR, Cloyd JM, *et al*. Management of Hepatocellular Carcinoma: A Review. JAMA Surgery. 2023; 158: 410–420. https://doi.org/10.1001/jamasurg.2022.7989.

[7] Li X, Ramadori P, Pfister D, Seehawer M, Zender L, Heikenwalder M. The immunological and metabolic landscape in primary and metastatic liver cancer. Nature Reviews. Cancer. 2021; 21: 541–557. https://doi.org/10.1038/s41568-021-00383-9.

[8] Maki H, Hasegawa K. Advances in the surgical treatment of liver cancer. Bioscience Trends. 2022; 16: 178–188. https://doi.org/10.5582/bst.2022.01245.

[9] Grewal T, Rentero C, Enrich C, Wahba M, Raabe CA, Rescher U. Annexin Animal Models-From Fundamental Principles to Translational Research. International Journal of Molecular Sciences. 2021; 22: 3439. https://doi.org/10.3390/ijms22073439.

[10] Li YZ, Wang YY, Huang L, Zhao YY, Chen LH, Zhang C. Annexin A protein family in atherosclerosis. Clinica Chimica Acta. 2022; 531: 406–417. https://doi.org/10.1016/j.cca.2022.05.009.

[11] de Souza Ferreira LP, da Silva RA, Gil CD, Geisow MJ. Annexin A1, A2, A5, and A6 involvement in human pathologies. Proteins. 2023; 91: 1191–1204. https://doi.org/10.1002/prot.26512.

[12] Jing J. The Relevance, Predictability, and Utility of Annexin A5 for Human Physiopathology. International Journal of Molecular Sciences. 2024; 25: 2865. https://doi.org/10.3390/ijms25052865.

[13] Woodward A, Faria GNF, Harrison RG. Annexin A5 as a targeting agent for cancer treatment. Cancer Letters. 2022; 547: 215857. https://doi.org/10.1016/j.canlet.2022.215857.

[14] Wang W, Liu D, Yao J, Yuan Z, Yan L, Cao B. ANXA5: A Key Regulator of Immune Cell Infiltration in Hepatocellular Carcinoma. Medical Science Monitor. 2024; 30: e943523. https://doi.org/10.12659/MSM.943523.

[15] Yang X, Zhu Y, Zhao X, Li JH, Xu D, Jia HL, *et al*. The Prognostic Comparison Between Hepatocellular Carcinoma with Portal Vein Tumor Thrombus and Bile Duct Cancer Thrombus After Liver Resection. Cancer Management and Research. 2020; 12: 12077–12086. https://doi.org/10.2147/CMAR.S278777.

[16] Herrera-López EE, Guerrero-Escalera D, Aguirre-Maldonado I, López-Hernández A, Montero H, Gutiérrez-Nava MA, *et al*. Annexins A2 and A5 are potential early biomarkers of hepatocarcinogenesis. Scientific Reports. 2023; 13: 6948. https://doi.org/10.1038/s41598-023-34117-8.

[17] Peng B, Guo C, Guan H, Liu S, Sun MZ. Annexin A5 as a potential marker in tumors. Clinica Chimica Acta. 2014; 427: 42–48. https://doi.org/10.1016/j.cca.2013.09.048.

[18] Giorgi C, Danese A, Missiroli S, Patergnani S, Pinton P. Calcium Dynamics as a Machine for Decoding Signals. Trends in Cell Biology. 2018; 28: 258–273. https://doi.org/10.1016/j.tcb.2018.01.002.

[19] Eisner D, Neher E, Taschenberger H, Smith G. Physiology of intracellular calcium buffering. Physiological Reviews. 2023; 103: 2767–2845. https://doi.org/10.1152/physrev.00042.2022.
[20] Zheng S, Wang X, Zhao D, Liu H, Hu Y. Calcium homeostasis and cancer: insights from endoplasmic reticulum-centered organelle communications. Trends in Cell Biology. 2023; 33: 312–323. https://doi.org/10.1016/j.tcb.2022.07.004.
[21] Singh J, Meena A, Luqman S. New frontiers in the design and discovery of therapeutics that target calcium ion signaling: a novel approach in the fight against cancer. Expert Opinion on Drug Discovery. 2023; 18: 1379–1392. https://doi.org/10.1080/17460441.2023.2251887.
[22] Wang J, Zhao H, Zheng L, Zhou Y, Wu L, Xu Y, *et al*. FGF19/SOCE/NFATc2 signaling circuit facilitates the self-renewal of liver cancer stem cells. Theranostics. 2021; 11: 5045–5060. https://doi.org/10.7150/thno.56369.
[23] Xie J, Pan H, Yao J, Zhou Y, Han W. SOCE and cancer: Recent progress and new perspectives. International Journal of Cancer. 2016; 138: 2067–2077. https://doi.org/10.1002/ijc.29840.
[24] Umemura M, Nakakaji R, Ishikawa Y. Physiological functions of calcium signaling via Orai1 in cancer. The Journal of Physiological Sciences. 2023; 73: 21. https://doi.org/10.1186/s12576-023-00878-0.
[25] Chang CL, Liou J. Homeostatic regulation of the PI(4,5)P2-Ca(2+) signaling system at ER-PM junctions. Biochimica et Biophysica Acta. 2016; 1861: 862–873. https://doi.org/10.1016/j.bbalip.2016.02.015.
[26] Sirover MA. Pleiotropic effects of moonlighting glyceraldehyde-3-phosphate dehydrogenase (GAPDH) in cancer progression, invasiveness, and metastases. Cancer Metastasis Reviews. 2018; 37: 665–676. https://doi.org/10.1007/s10555-018-9764-7.
[27] Kodakandla G, Akimzhanov AM, Boehning D. Regulatory mechanisms controlling store-operated calcium entry. Frontiers in Physiology. 2023; 14: 1330259. https://doi.org/10.3389/fphys.2023.1330259.
[28] Liang X, Zhang N, Pan H, Xie J, Han W. Development of Store-Operated Calcium Entry-Targeted Compounds in Cancer. Frontiers in Pharmacology. 2021; 12: 688244. https://doi.org/10.3389/fphar.2021.688244.
[29] Prakriya M, Lewis RS. Store-Operated Calcium Channels. Physiological Reviews. 2015; 95: 1383–1436. https://doi.org/10.1152/physrev.00020.2014.
[30] Lu F, Li Y, Lin S, Cheng H, Yang S. Spatiotemporal regulation of store-operated calcium entry in cancer metastasis. Biochemical Society Transactions. 2021; 49: 2581–2589. https://doi.org/10.1042/BST20210307.
[31] Hammad AS, Machaca K. Store Operated Calcium Entry in Cell Migration and Cancer Metastasis. Cells. 2021; 10: 1246. https://doi.org/10.3390/cells10051246.
[32] Sun Y, Thapa N, Hedman AC, Anderson RA. Phosphatidylinositol 4,5-bisphosphate: targeted production and signaling. BioEssays. 2013; 35: 513–522. https://doi.org/10.1002/bies.201200171.
[33] Zhu X, Jin C, Pan Q, Hu X. Determining the quantitative relationship between glycolysis and GAPDH in cancer cells exhibiting the Warburg effect. The Journal of Biological Chemistry. 2021; 296: 100369. https://doi.org/10.1016/j.jbc.2021.100369.
[34] Seidler NW. Basic biology of GAPDH. Advances in Experimental Medicine and Biology. 2013; 985: 1–36. https://doi.org/10.1007/978-94-007-4716-6_1.
[35] Wang J, Yu X, Cao X, Tan L, Jia B, Chen R, *et al*. GAPDH: A common housekeeping gene with an oncogenic role in pan-cancer. Computational and Structural Biotechnology Journal. 2023; 21: 4056–4069. https://doi.org/10.1016/j.csbj.2023.07.034.
[36] Talwar D, Miller CG, Grossmann J, Szyrwiel L, Schwecke T, Demichev V, *et al*. The GAPDH redox switch safeguards reductive capacity and enables survival of stressed tumour cells. Nature Metabolism. 2023; 5: 660–676. https://doi.org/10.1038/s42255-023-00781-3.
[37] Stelzer G, Rosen N, Plaschkes I, Zimmerman S, Twik M, Fishilevich S, *et al*. The GeneCards Suite: From Gene Data Mining to Disease Genome Sequence Analyses. Current Protocols in Bioinformatics. 2016; 54: 1.30.1–1.30.33. https://doi.org/10.1002/cpbi.5.
[38] Shannon P, Markiel A, Ozier O, Baliga NS, Wang JT, Ramage D, *et al*. Cytoscape: a software environment for integrated models of biomolecular interaction networks. Genome Research. 2003; 13: 2498–2504. https://doi.org/10.1101/gr.1239303.
[39] Mancinelli S, Turcato A, Kisslinger A, Bongiovanni A, Zazzu V, Lanati A, *et al*. Design of transfections: Implementation of design of experiments for cell transfection fine tuning. Biotechnology and Bioengineering. 2021; 118: 4488–4502. https://doi.org/10.1002/bit.27918.
[40] Dekevic G, Tasto L, Czermak P, Salzig D. Statistical experimental designs to optimize the transient transfection of HEK 293T cells and determine a transfer criterion from adherent cells to larger-scale cell suspension cultures. Journal of Biotechnology. 2022; 346: 23–34. https://doi.org/10.1016/j.jbiotec.2022.01.004.
[41] Li Y, Jin L, Li Y, Qian J, Wang Z, Zheng X, *et al*. Lysophosphatidic Acid Improves Human Sperm Motility by Enhancing Glycolysis and Activating L-Type Calcium Channels. Frontiers in Endocrinology. 2022; 13: 896558. https://doi.org/10.3389/fendo.2022.896558.
[42] Tang Y, Rijal R, Zimmerhanzel DE, McCullough JR, Cadena LA, Gomer RH. An Autocrine Negative Feedback Loop Inhibits Dictyostelium discoideum Proliferation through Pathways Including IP3/Ca^{2+}. mBio. 2021; 12: e0134721. https://doi.org/10.1128/mBio.01347-21.
[43] Zheng J, Wang Y, Zhou Y, Li Z, Yang L, Gao J, *et al*. Augmentation of hepatocellular carcinoma malignancy by annexin A5 through modulation of invasion and angiogenesis. Scandinavian Journal of Gastroenterology. 2024; 59: 939–953. https://doi.org/10.1080/00365521.2024.2353103.
[44] Peng B, Liu S, Guo C, Sun X, Sun MZ. ANXA5 level is linked to in vitro and in vivo tumor malignancy and lymphatic metastasis of murine hepatocarcinoma cell. Future Oncology. 2016; 12: 31–42. https://doi.org/10.2217/fon.15.289.
[45] Li Y, Li E, Zheng W, Shi J, Yu S, Zhang X, *et al*.. Newly Established Anoikis-Associated Genes Predict the Prognosis of Hepatocellular Carcinoma. Journal of Hepatocellular Carcinoma. 2025; 12: 2017–2034. https://doi.org/10.2147/JHC.S533398.
[46] Xue G, Hao LQ, Ding FX, Mei Q, Huang JJ, Fu CG, *et al*. Expression of annexin a5 is associated with higher tumor stage and poor prognosis in colorectal adenocarcinomas. Journal of Clinical Gastroenterology. 2009; 43: 831–837. https://doi.org/10.1097/MCG.0b013e31819cc731.
[47] Yang D, Chen H, Zhou Z, Guo J. ANXA5 predicts prognosis and immune response and mediates proliferation and migration in head and neck squamous cell carcinoma. Gene. 2024; 931: 148867. https://doi.org/10.1016/j.gene.2024.148867.
[48] Yao X, Qi X, Wang Y, Zhang B, He T, Yan T, *et al*. Identification and Validation of an Annexin-Related Prognostic Signature and Therapeutic Targets for Bladder Cancer: Integrative Analysis. Biology. 2022; 11: 259. https://doi.org/10.3390/biology11020259.
[49] Zhou T, Zhang X, Song Y, Ding L, Huang X, Zhang L, *et al*. Annexin A5 is a novel prognostic biomarker in oral squamous cell carcinoma. Journal of Oral Pathology & Medicine. 2024; 53: 538–543. https://doi.org/10.1111/jop.13567.

[50] Sun Y, Wu L, Zhong Y, Zhou K, Hou Y, Wang Z, *et al*. Single-cell landscape of the ecosystem in early-relapse hepatocellular carcinoma. Cell. 2021; 184: 404–421.e16. https://doi.org/10.1016/j.cell.2020.11.041.

[51] Koshy A. Evolving Global Etiology of Hepatocellular Carcinoma (HCC): Insights and Trends for 2024. Journal of Clinical and Experimental Hepatology. 2025; 15: 102406. https://doi.org/10.1016/j.jceh.2024.102406.

[52] Geh D, Anstee QM, Reeves HL. NAFLD-Associated HCC: Progress and Opportunities. Journal of Hepatocellular Carcinoma. 2021; 8: 223–239. https://doi.org/10.2147/JHC.S272213.

[53] Singal AG, Kanwal F, Llovet JM. Global trends in hepatocellular carcinoma epidemiology: implications for screening, prevention and therapy. Nature Reviews. Clinical Oncology. 2023; 20: 864–884. https://doi.org/10.1038/s41571-023-00825-3.

[54] Riddiough GE, Jalal Q, Perini MV, Majeed AW. Liver regeneration and liver metastasis. Seminars in Cancer Biology. 2021; 71: 86–97. https://doi.org/10.1016/j.semcancer.2020.05.012.

[55] Berridge MJ. Inositol trisphosphate and calcium signalling mechanisms. Biochimica et Biophysica Acta. 2009; 1793: 933–940. https://doi.org/10.1016/j.bbamcr.2008.10.005.

[56] Chini EN, Dousa TP. Differential effect of glycolytic intermediaries upon cyclic ADP-ribose-, inositol 1',4',5'-trisphosphate-, and nicotinate adenine dinucleotide phosphate-induced Ca(2+) release systems. Archives of Biochemistry and Biophysics. 1999; 370: 294–299. https://doi.org/10.1006/abbi.1999.1373.

[57] Xiang L, Wei H, Ye W, Wu S, Xie G. Prolyl hydroxylase 2 inhibits glycolytic activity in colorectal cancer via the NF-κB signaling pathway. International Journal of Oncology. 2024; 64: 2. https://doi.org/10.3892/ijo.2023.5590.

[58] Shapovalov G, Gordienko D, Prevarskaya N. Store operated calcium channels in cancer progression. International Review of Cell and Molecular Biology. 2021; 363: 123–168. https://doi.org/10.1016/bs.ircmb.2021.02.016.

[59] Wei J, Deng Y, Ye J, Luo Y, Weng J, He Q, *et al*. Store-operated Ca^{2+} entry as a key oncogenic Ca^{2+} signaling driving tumor invasion-metastasis cascade and its translational potential. Cancer Letters. 2021; 516: 64–72. https://doi.org/10.1016/j.canlet.2021.05.036.

[60] Emrich SM, Yoast RE, Trebak M. Physiological Functions of CRAC Channels. Annual Review of Physiology. 2022; 84: 355–379. https://doi.org/10.1146/annurev-physiol-052521-013426.

[61] Kim OH, Kang GH, Hur J, Lee J, Jung Y, Hong IS, *et al*. Externalized phosphatidylinositides on apoptotic cells are eat-me signals recognized by CD14. Cell Death and Differentiation. 2022; 29: 1423–1432. https://doi.org/10.1038/s41418-022-00931-2.

[62] Khalaji A, Yancheshmeh FB, Farham F, Khorram A, Sheshbolouki S, Zokaei M, *et al*. Don't eat me/eat me signals as a novel strategy in cancer immunotherapy. Heliyon. 2023; 9: e20507. https://doi.org/10.1016/j.heliyon.2023.e20507.

[63] Hafezi S, Rahmani M. Targeting BCL-2 in Cancer: Advances, Challenges, and Perspectives. Cancers. 2021; 13: 1292. https://doi.org/10.3390/cancers13061292.

[64] King LE, Hohorst L, García-Sáez AJ. Expanding roles of BCL-2 proteins in apoptosis execution and beyond. Journal of Cell Science. 2023; 136: jcs260790. https://doi.org/10.1242/jcs.260790.

[65] Palabiyik AA. The role of Bcl-2 in controlling the transition between autophagy and apoptosis (Review). Molecular Medicine Reports. 2025; 32: 172. https://doi.org/10.3892/mmr.2025.13537.

[66] Hosseini-Khah Z, Babaei MR, Tehrani M, Cucchiarini M, Madry H, Ajami A, *et al*. SOX2 and Bcl-2 as a Novel Prognostic Value in Hepatocellular Carcinoma Progression. Current Oncology. 2021; 28: 3015–3029. https://doi.org/10.3390/curroncol28040264.

[67] Donne R, Lujambio A. The liver cancer immune microenvironment: Therapeutic implications for hepatocellular carcinoma. Hepatology. 2023; 77: 1773–1796. https://doi.org/10.1002/hep.32740.

[68] Zhou D, Duan Z, Li Z, Ge F, Wei R, Kong L. The significance of glycolysis in tumor progression and its relationship with the tumor microenvironment. Frontiers in Pharmacology. 2022; 13: 1091779. https://doi.org/10.3389/fphar.2022.1091779.

[69] Zhou Q, Nguyen TTT, Mun JY, Siegelin MD, Greene LA. DPEP Inhibits Cancer Cell Glucose Uptake, Glycolysis and Survival by Upregulating Tumor Suppressor TXNIP. Cells. 2024; 13: 1025. https://doi.org/10.3390/cells13121025.

[70] Yi F, Long S, Yao Y, Fu K . A Novel Signature Composed of Hypoxia, Glycolysis, Lactylation Related Genes to Predict Prognosis and Immunotherapy in Hepatocellular Carcinoma. Frontiers in bioscience (Landmark edition). 2025; 30: 33422. https://doi.org/10.31083/FBL33422.

[71] Yang Y, Ren P, Liu X, Sun X, Zhang C, Du X, *et al*. PPP1R26 drives hepatocellular carcinoma progression by controlling glycolysis and epithelial-mesenchymal transition. Journal of Experimental & Clinical Cancer Research. 2022; 41: 101. https://doi.org/10.1186/s13046-022-02302-8.

[72] Kooshan Z, Cárdenas-Piedra L, Clements J, Batra J. Glycolysis, the sweet appetite of the tumor microenvironment. Cancer Letters. 2024; 600: 217156. https://doi.org/10.1016/j.canlet.2024.217156.

[73] Chaudhary P, Srivastava P, Manna PP. Effector Functions of Dendritic Cells in Cancer: Role of Cytotoxicity and Growth Inhibition. International Journal of Molecular Sciences. 2024; 29: 293. https://doi.org/10.31083/j.fbl2908293.

[74] Saeed AF. Tumor-Associated Macrophages: Polarization, Immunoregulation, and Immunotherapy. Cells. 2025; 14: 741. https://doi.org/10.3390/cells14100741.

[75] Xu F, Guo M, Huang W, Feng L, Zhu J, Luo K, *et al*. Annexin A5 regulates hepatic macrophage polarization via directly targeting PKM2 and ameliorates NASH. Redox Biology. 2020; 36: 101634. https://doi.org/10.1016/j.redox.2020.101634.

[76] Frey B, Munoz LE, Pausch F, Sieber R, Franz S, Brachvogel B, *et al*. The immune reaction against allogeneic necrotic cells is reduced in Annexin A5 knock out mice whose macrophages display an anti-inflammatory phenotype. Journal of Cellular and Molecular Medicine. 2009; 13: 1391–1399. https://doi.org/10.1111/j.1582-4934.2008.00395.x.

[77] Jia Z, Kang B, Dong Y, Fan M, Li W, Zhang W. Annexin A5 Derived from Cell-free Fat Extract Attenuates Osteoarthritis via Macrophage Regulation. International Journal of Biological Sciences. 2024; 20: 2994–3007. https://doi.org/10.7150/ijbs.92802.

[78] Kang B, Jia Z, Li W, Zhang W. Recombinant Human Annexin A5 Ameliorates Localized Scleroderma by Inhibiting the Activation of Fibroblasts and Macrophages. Pharmaceutics. 2025; 17: 986. https://doi.org/10.3390/pharmaceutics17080986.

[79] Oura K, Morishita A, Tani J, Masaki T. Tumor Immune Microenvironment and Immunosuppressive Therapy in Hepatocellular Carcinoma: A Review. International Journal of Molecular Sciences. 2021; 22: 5801. https://doi.org/10.3390/ijms22115801.